Cell Reports
Medicine

Article

Integrative proteomics identifies a conserved Aβ amyloid responsome, novel plaque proteins, and pathology modifiers in Alzheimer's disease

Graphical abstract

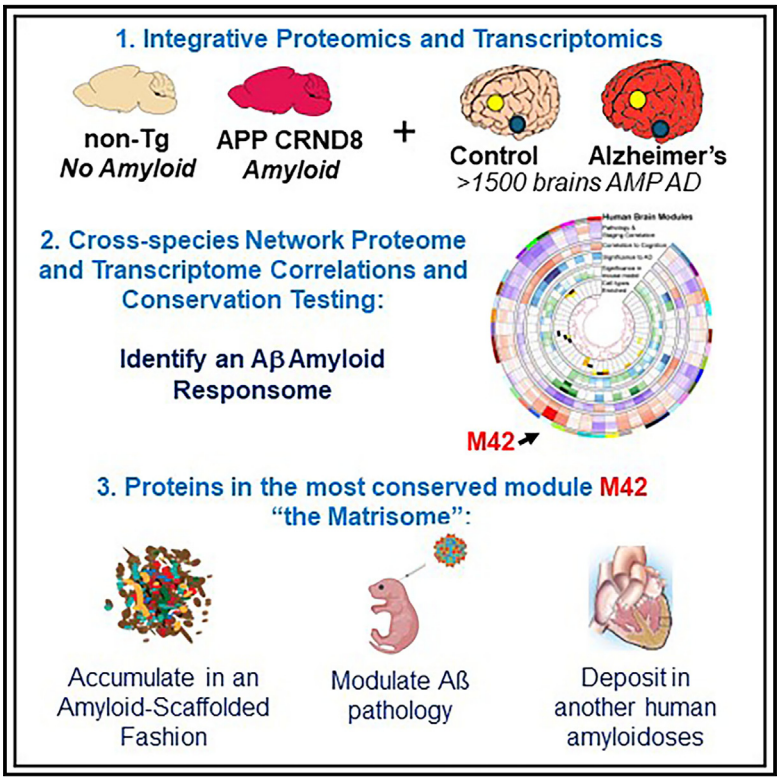

Highlights

- Cross-species brain proteomic data identify a conserved Aβ amyloid responsome
- Proteins in a conserved module, M42, are pathologically related to amyloid deposits
- Expression of M42 proteins, midkine or pleiotrophin, increases amyloid deposition
- Amyloid-scaffolded accumulation of M42 proteins may contribute to AD pathology

Authors

Yona Levites, Eric B. Dammer, Yong Ran, ..., Stefan Prokop, Nicholas T. Seyfried, Todd E. Golde

Correspondence

sprokop@ufl.edu (S.P.), nseyfri@emory.edu (N.T.S.), tgolde@emory.edu (T.E.G.)

In brief

Levites et al. compare the brain proteomes of Alzheimer's disease (AD) and amyloid-depositing mice to identify an amyloid "responsome." They demonstrate that the conserved protein network, module M42, is linked to amyloid pathology. Overexpression of M42 proteins, midkine and pleiotrophin, increases amyloid deposition, indicating they are pathology modifiers and therapeutic targets.

Levites et al., 2024, Cell Reports Medicine 5, 101669
August 20, 2024
https://doi.org/10.1016/j.xcrm.2024.101669

CellPress

Cell Reports Medicine

CellPress
OPEN ACCESS

Article

Integrative proteomics identifies a conserved Aβ amyloid responsome, novel plaque proteins, and pathology modifiers in Alzheimer's disease

Yona Levites,[1,4,5,20] Eric B. Dammer,[2,4,5,20] Yong Ran,[1,4,5] Wangchen Tsering,[6,7,8] Duc Duong,[2,4,5] Measho Abreha,[2,4,5] Joshna Gadhavi,[2,4,5] Kiara Lolo,[6,7,8] Jorge Trejo-Lopez,[6,7,8] Jennifer Phillips,[6,7,8] Andrea Iturbe,[8,9] Aya Erquizi,[8,9] Brenda D. Moore,[1,4,5] Danny Ryu,[1,4,5] Aditya Natu,[2,4,5] Kristy Dillon,[7,8,9] Jose Torrellas,[7,8,9] Corey Moran,[7,8,9] Thomas Ladd,[7,8] Farhana Afroz,[1,4,5] Tariful Islam,[1,4,5] Jaishree Jagirdar,[13] Cory C. Funk,[14] Max Robinson,[14] Srikant Rangaraju,[19] David R. Borchelt,[7,8,9] Nilüfer Ertekin-Taner,[11,12] Jeffrey W. Kelly,[15] Frank L. Heppner,[16,17,18] Erik C.B. Johnson,[3,4,5] Karen McFarland,[1,4,5] Allan I. Levey,[3,4,5] Stefan Prokop,[6,7,8,10,*] Nicholas T. Seyfried,[2,4,5,*] and Todd E. Golde[1,3,4,5,21,*]

[1]Department of Pharmacology and Chemical Biology, School of Medicine, Emory University, Atlanta, GA, USA
[2]Department of Biochemistry, School of Medicine, Emory University, Atlanta, GA, USA
[3]Department of Neurology, School of Medicine, Emory University, Atlanta, GA, USA
[4]Goizueta Brain Health Institute and Alzheimer's Disease Research Center, Emory University School of Medicine, Atlanta, GA, USA
[5]Center for Neurodegenerative Disease Center, Emory University School of Medicine, Atlanta, GA, USA
[6]Department of Pathology, College of Medicine, University of Florida, Gainesville, FL, USA
[7]Evelyn F. and William L. McKnight Brain Institute, University of Florida, Gainesville, FL, USA
[8]Center for Translational Research in Neurodegenerative Disease, University of Florida, Gainesville, FL, USA
[9]Department of Neuroscience, College of Medicine, University of Florida, Gainesville, FL, USA
[10]Department of Neurology, College of Medicine, University of Florida, Gainesville, FL, USA
[11]Mayo Clinic, Department of Neuroscience, Jacksonville, FL, USA
[12]Mayo Clinic, Department of Neurology, Jacksonville, FL, USA
[13]Department of Pathology and Laboratory Medicine, Emory University Hospital, Atlanta, GA, USA
[14]Institute for Systems Biology, Seattle, WA, USA
[15]Department of Chemistry and The Skaggs Institute for Chemical Biology, The Scripps Research Institute, La Jolla, CA, USA
[16]Department of Neuropathology, Charité – Universitätsmedizin Berlin, Corporate Member of Freie Universität Berlin and Humboldt-Universität zu Berlin, 110117 Berlin, Germany
[17]German Center for Neurodegenerative Diseases (DZNE) Berlin, 110117 Berlin, Germany
[18]Cluster of Excellence, NeuroCure, Charitéplatz, 110117 Berlin, Germany
[19]Department of Neurology, Yale University, New Haven, CT, USA
[20]These authors contributed equally
[21]Lead contact
*Correspondence: sprokop@ufl.edu (S.P.), nseyfri@emory.edu (N.T.S.), tgolde@emory.edu (T.E.G.)
https://doi.org/10.1016/j.xcrm.2024.101669

SUMMARY

Alzheimer's disease (AD) is a complex neurodegenerative disorder that develops over decades. AD brain proteomics reveals vast alterations in protein levels and numerous altered biologic pathways. Here, we compare AD brain proteome and network changes with the brain proteomes of amyloid β (Aβ)-depositing mice to identify conserved and divergent protein networks with the conserved networks identifying an Aβ amyloid responsome. Proteins in the most conserved network (M42) accumulate in plaques, cerebrovascular amyloid (CAA), and/or dystrophic neuronal processes, and overexpression of two M42 proteins, midkine (Mdk) and pleiotrophin (PTN), increases the accumulation of Aβ in plaques and CAA. M42 proteins bind amyloid fibrils *in vitro*, and MDK and PTN co-accumulate with cardiac transthyretin amyloid. M42 proteins appear intimately linked to amyloid deposition and can regulate amyloid deposition, suggesting that they are pathology modifiers and thus putative therapeutic targets. We posit that amyloid-scaffolded accumulation of numerous M42+ proteins is a central mechanism mediating downstream pathophysiology in AD.

INTRODUCTION

The amyloid cascade hypothesis serves as a foundational framework for comprehending the pathogenesis of Alzheimer's disease (AD).[1,2] Evidence from anti-amyloid immunotherapies, developed based on this hypothesis, offers the initial therapeutic validation, affirming that Aβ deposition plays a role in the AD pathogenic cascade.[3–5] Despite extensive investigation, significant gaps in our understanding of AD pathogenesis remain.[2,6,7] The initial notion of a purely linear amyloid cascade is now recognized

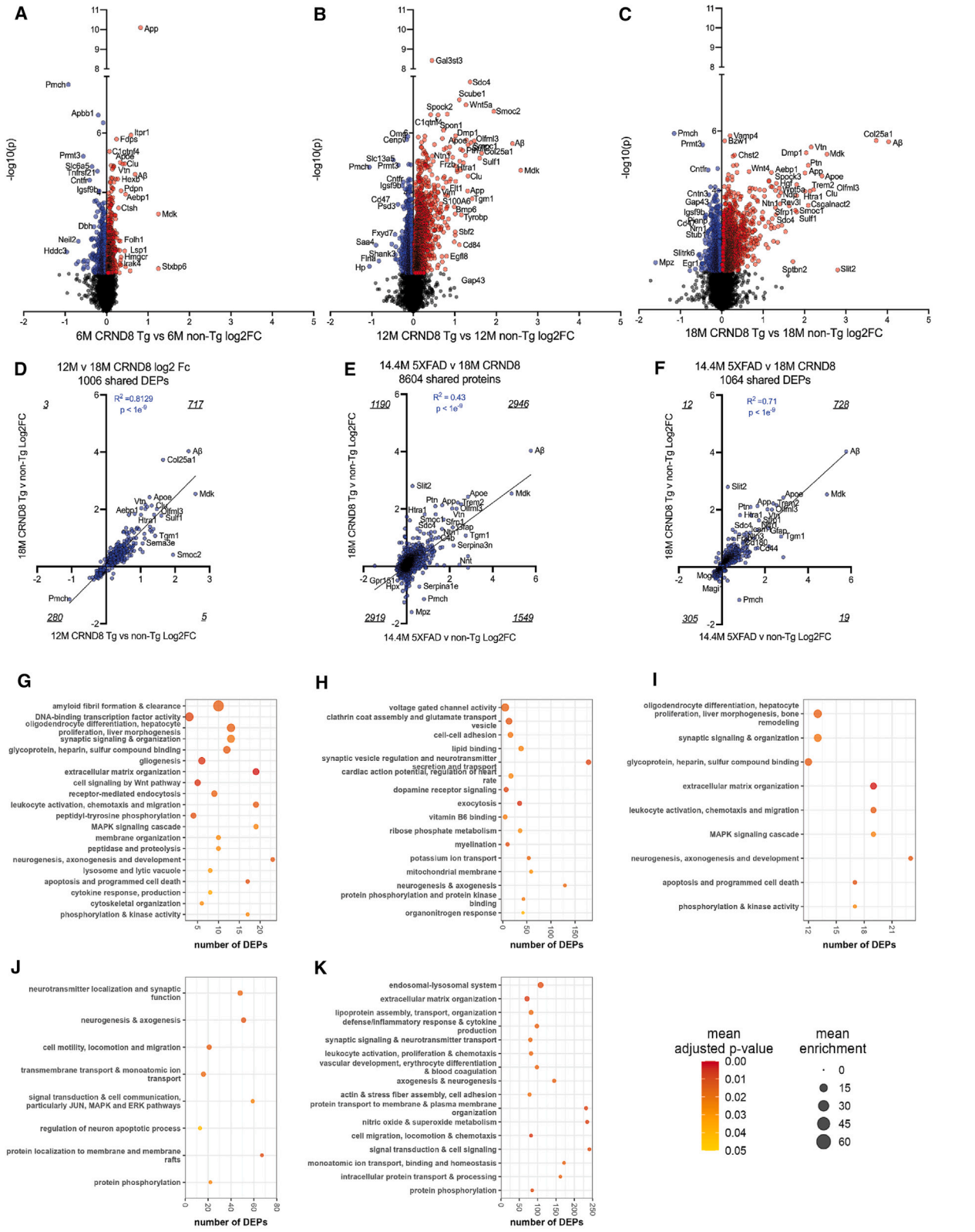

(legend on next page)

as overly simplistic. Multi-omic studies have unveiled the vast complexity of changes occurring over decades in the brains of individuals as various AD hallmark pathologies emerge.[6,8–23]

Typically, systems-level omic studies cannot establish cause-and-effect relationships. However, by combining strong correlational inference with omics obtained from different AD stages, we can generate hypotheses regarding causality or the role of these changes in the disease. To determine whether omic-level changes play a fundamental role in pathogenesis, it is essential to (1) compare the data across related disorders and disease models, (2) integrate the data with genetic risk and biomarker information, and (3) directly manipulate the levels of the altered proteins or RNAs in various model systems to observe their impact on pathophysiology potentially relevant to human AD.

Here, we performed quantitative tandem mass tag mass spectrometry (TMT-MS)-based proteomic analyses of the brains from CRND8 mice[24] at various ages and compared these findings to brain proteome data from 5XFAD mice[25] and human AD, asymptomatic AD (AsymAD, i.e., individuals with neuropathologic criteria of AD but normal cognition before death), and control brain from multiple cohorts.[8,26,27] We find robust, highly significant, correlations in global proteome changes in human AD and AsymAD brains compared to the transgenic (Tg) mouse models and both conserved and divergent network module changes. Proteins that map to the conserved M42 matrisome module accumulate in Aβ plaques, cerebrovascular amyloid (CAA), and/or dystrophic neuronal processes with overexpression of midkine (Mdk) and pleiotrophin (PTN) in CRND8 mice leading to accelerated accumulation of Aβ in plaques and CAA. M42 proteins exhibit binding to fibrillar Aβ and non-human amyloid fibrils *in vitro*, and both MDK and PTN co-accumulate in cardiac transthyretin (TTR) amyloid. This contextualized understanding of AD proteomic changes and their interplay with amyloid deposition provides valuable insights into AD pathogenesis. More specifically, they suggest that antagonizing MDK and/or PTN binding to amyloid could be a therapeutic strategy.

RESULTS

Deep TMT-MS proteomes from 6, 12, and 18M CRND8 APP mice

We generated TMT-MS proteomic data from the 8 M urea extracts of brains from 6-, 12-, and 18-month CRND8 mice and non-transgenic (non-Tg) controls (Figure 1; Tables S1, S2, S3, and S4). These data identify over 1,000 differentially expressed proteins (DEPs) at each age, with an age-dependent increase in DEPs (Figure 1C). Proteomic changes in 12 and 18-month cohorts are highly reproducible (Figure 1D). We also compared the CRND8 18-month data to 14.5-month 5XFAD mice brain proteomes,[28] revealing robust correlations for the shared proteins and DEPs (Figures 1E and 1F). Thus, small cohorts of mice with varying levels of amyloid deposition enable robust, reliable detection of proteomic alterations.

Both full-length APP and specific peptides mapping to the human Aβ peptide sequence distinguish CRND8 Tg from non-Tg mice in all cohorts, consistent with human transgene expression and increasing deposition of Aβ (Figures 1A–1C; Table S1). Other proteins previously shown to interact with APP (e.g., Apbb1 [Fe65], Vac14, Rufy2, and Tnfrsf21) are also altered at various ages in the CRND8 proteome.[29–31] Top gene ontology (GO) terms for the DEPs increased in all cohorts highlight heparin and glycosaminoglycan binding, amyloid fibril formation and regulation, vacuolar and lysosomal transport, immune phagosome and vesicular and lysosomal transport, integrin binding, and extracellular matrix organization (Figure 1G). Top ontology terms for decreased DEPs in all cohorts highlight impacts on lipid binding, synaptic vesicle regulation and neurotransmitter release, mitochondrial membrane, and neurogenesis and axogenesis (Figure 1H).

In the 12 and 18-month cohorts there is an appreciable rightward shift in the volcano plots reflecting proteins that show an age-dependent increase in abundance. These changes likely reflect an evolving Aβ amyloid responsome. A subset of the proteins that show the largest fold change increase has been observed to be altered in other APP mouse models and in humans[8,9,13,17,28,32,33] (Table S1). However, in this study, using older CRND8 mice, which have extensive parenchymal amyloid deposition in the forebrain and hippocampus and CAA deposition in the cerebellum, we appear to have detected a more comprehensive picture of the alterations in the proteome in response to Aβ deposition in the brain. GO and Kyoto Encyclopedia of Genes and Genomes terms for the DEPs that are significantly altered in the 18M CRND8 cohort relative to the change observed in the 6-month cohort highlight the many complex biological processes in this putative responsome (Figures 1I–1K).

Figure 1. TMT-MS analysis and gene ontologies of CRND8 mice versus non-Tg brains

(A) Volcano plot of 6-month cohort.
(B) Volcano plot of 12-month cohort.
(C) Volcano plot of 18-month cohort.
(D) Correlation of CRND8 brain DEPs between the 12-month (x) and 18-month cohorts (y). Numbers underlined and in italics list the number of genes in each quadrant of this and other x-y plots.
(E) Correlation of brain proteins between the 5XFAD 18-month (x) and CRND8 18-month cohorts (y).
(F) Correlation of brain DEPs between the 5XFAD 18-month (x) and CRND8 18-month cohorts (y).
(G) Thematic grouping of gene ontology categories of DEPs increased in all CRND8 cohorts.
(H) Thematic grouping of gene ontology categories of DEPs decreased in all CRND8 cohorts.
(I) Thematic grouping of gene ontology categories of DEPs (log2FC > 0.2) and increased by >2-fold in the 18-month CRND8 cohort relative to the 6-month cohort.
(J) Thematic grouping of gene ontology categories of DEPs (log2FC > 1) and increased by >2-fold in the 18-month CRND8 cohort relative to the 6-month cohort.
(K) Thematic grouping of gene ontology categories of DEPs (log2FC < −0.1) and decreased by >2-fold in the 18-month CRND8 cohort relative to the 6-month cohort. The data underlying this figure are found in Table S1. Additional proteomic data for the CRND8 studies are found in Tables S2, S3, and S4. Lists of all genes used for gene ontology analyses are provided in Table S7.

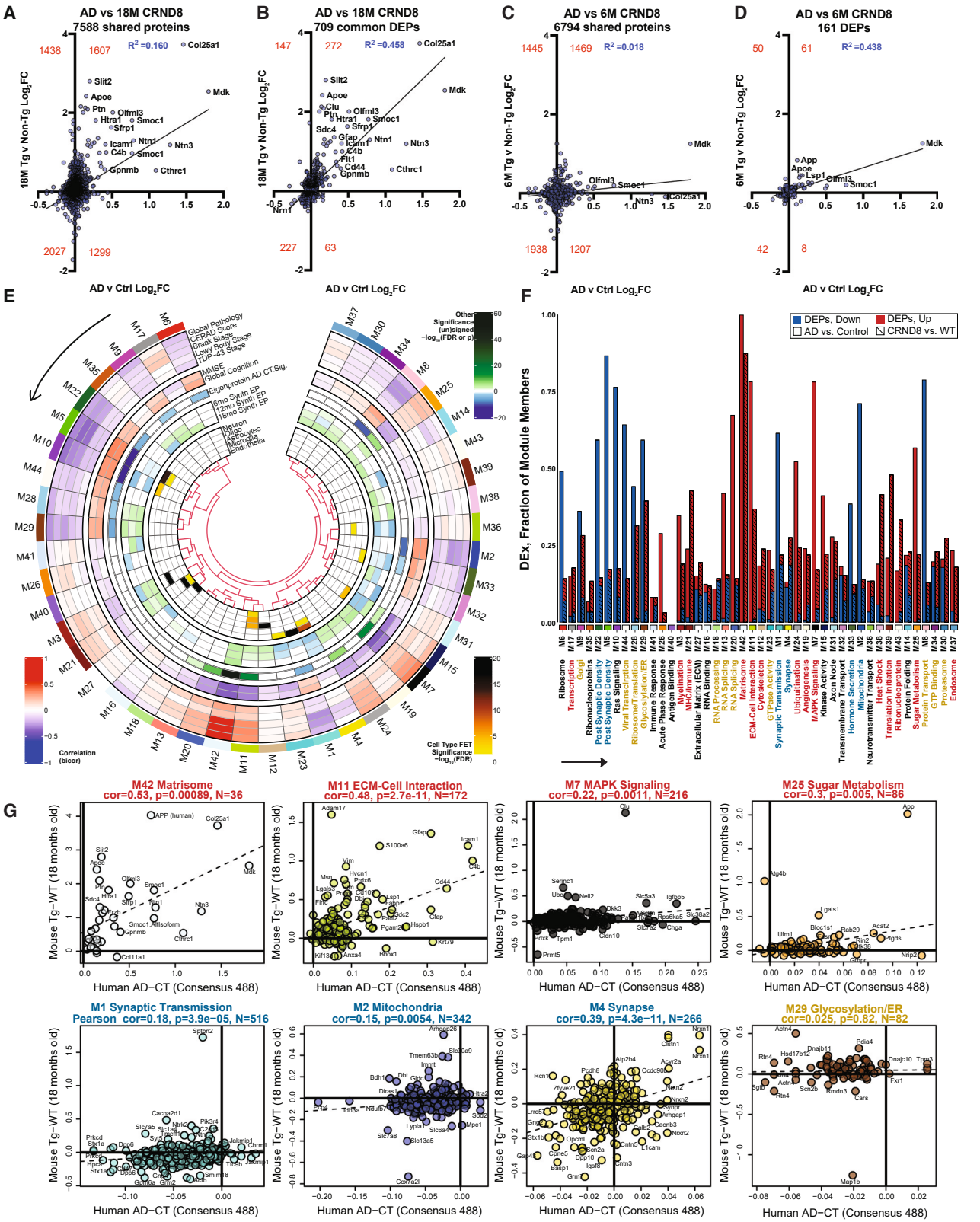

(legend on next page)

Integration of the AD human brain and CRND8 mouse brain proteome reveals both conserved and divergent changes

To understand changes in protein levels between human AD and control brains and CRND8 Tg and non-Tg mouse brains, we leveraged an extensive proteomic network analysis of dorsal lateral prefrontal cortex (DLFPC-1) and the resulting network module framework from AD and control brains that has been previously published.[8] This network was constructed using the weighted gene co-expression network algorithm (WGCNA) and consists of 44 modules reflecting multiple biological and cell type processes. Globally, when levels of shared proteins are compared between the 18M CRND8 Tg and non-Tg brains and AD and control brains, there is a significant correlation (Figure 2A); the strength of the correlation is increased when filtering on DEPs (Figure 2B). Comparison of the 6-month CRND8 proteome changes with AD reveals a much weaker correlation for all overlapping proteins, but still a strong correlation for shared DEPs (Figure 2D). Notably, the correlation for proteins is stronger than for the correlation between protein-coding mRNAs in 20-month-old CRND8 mice vs. non-Tg mice brains and human AD and control brain temporal cortex (Figures S1A and S1B).[11,34]

There is a robust correlation between AD and AsymAD in the published DLFPC-1 data for all shared proteins and the shared DEPs. However, on average, the log2FC relative to control is reduced ~40%–50% for AsymAD relative to AD (Figures S1C and S1D). Correlations between the 18-month CRND8 brain proteomes and the AsymAD proteome are thus robust (Figures S1E and S1F). To ensure the human DLFPC-1 AD is broadly representative, we compared it to two other proteomic datasets. DLFPC-2 data consist of proteomes from 633 AD and 234 controls, and superior temporal gyrus data consist of proteomes from 177 AD and 86 controls.[26,27] These AD brain proteomes show robust correlations with the original DLFPC-1 proteome (Figure S1G) and CRND8 18-month proteomes (Figures S1H and S1I).

Correlations of all proteins shared within the human modules revealed modules with high overall correlations in terms of directionality and magnitude of changes and modules with negative correlations (Figure 2E). When we assess the CRND8 mouse proteome changes by evaluating the DEPs and preservation of direction of change within the human AD brain module structure (Figure 2F), there are multiple modules in which there is a high degree of preservation between the CRND8 and human proteome. There are also modules for which many DEPs are discordant, as well as modules where the preservation of directionality is mixed. Examples of the cross-species correlations observed between all proteins within individual modules detected between the human AD proteome and the 18-month CRND8 proteome are shown in Figure 2G. These correlations range from robust and significant (M42, M11, and M4) to modest but significant (M7, M25, and M2) to absent (M29).

Human AD protein modules show an increased magnitude of change in aged CRND8 brains

We assessed the synthetic eigenprotein levels in the CRND8 cohorts to evaluate how proteins within these modules change over age and how they compare to eigenprotein changes in human AsymAD and AD (Figure 3). Eigenproteins are calculated for each module of the human network as the first principal component of variance of all module members. The top 20% of the most correlated human module hubs found in mouse are used to calculate a first principal component in synthetic mouse eigengenes. Across many modules, there is an increase in the magnitude of the eigenprotein change with preserved directionality as CRND8 mice age (e.g., M42, M11, M21, M7, M1, and M9). Other modules show different patterns of change with age. For example, M15 (kinase activity) and M2 (mitochondria) show increased eigenproteins in the 6-month cohort and then decreased eigenproteins in the older cohorts, whereas M3 (myelination)

Figure 2. Integrated mouse and human brain proteome comparison reveals concordant and discordant changes between CRND8 mice brains and human AD

(A) 7,588 mouse orthologs of human brain proteins quantified in both proteomes of the consensus human AD brain proteome (AD vs. Ctrl) and the 18-month mice (CRND8 Tg vs. non-Tg) are compared by their effect size (log2FC in human (x) vs. mouse (y). Numbers underlined and in italics list the number of genes in each quadrant of this and other x-y plots.

(B) Proteins in A were filtered to retain only orthologs nominally significantly changed in both human and the 18-month mice.

(C) 6,794 mouse orthologs of human brain proteins quantified in both proteomes of the consensus human AD brain proteome (AD vs. control) and the 6-month mice (CRND8 Tg vs. non-Tg) are compared by their effect size in human (x) vs. mouse (y).

(D) Proteins in C were filtered to retain only orthologs nominally significantly changed in both human and the 6-month mice.

(E) The human AD consensus brain network mapped to the CRND8 mouse brain shows trait correlations in human (outer two tracks; red, positive correlation to white, no correlation, to blue, negative correlation), effect size directionality and significance for AD (third track from the outside), the effect size directionalities and significance for CRND8 Tg vs. non-Tg at 6, 12, and 18-month in cognate mouse synthetic modules (Synth eigenproteins, EP), and hypergeometric overlap significance with cell type marker lists, indicating cell type enrichment of modules in the innermost track. Modules are numbered M1 to M44, ordered by bicor correlation relatedness (dendrogram), from M6, top left, to M37, top right, in a counterclockwise direction. Statistical values underlying the heatmap are in Table S6.

(F) The 44 consensus modules were assessed for a fraction of module member proteins achieving differentially expressed protein (DEP) status, discerning decreased DEPs in disease or Tg as blue, and increased DEPs as red in a stacked bar chart. Human and mouse bars for each module are shown side-by-side and left and right, respectively, above each module description. Descriptions below the numbered identifiers match the order of modules presented in the previous panel. The color of the description text indicates concordant increases (red), decreases (blue), discordant in direction of change (gold), or non-concordant (black).

(G) Mouse orthologs CRND8 18-month Tg vs. non-Tg effect sizes are compared to the AD vs. control effect sizes, module by module, with selected modules shown here. Pearson correlation rho and Student's significance of correlation are provided along with the number of orthologs mapping to each consensus module plotted. Text color of each module plot title matches the scheme described for the previous panel. Visualization for human-mouse correlations of all 44 modules' proteins across human and mouse is available online, as described in STAR Methods and on .synapse.org [35]

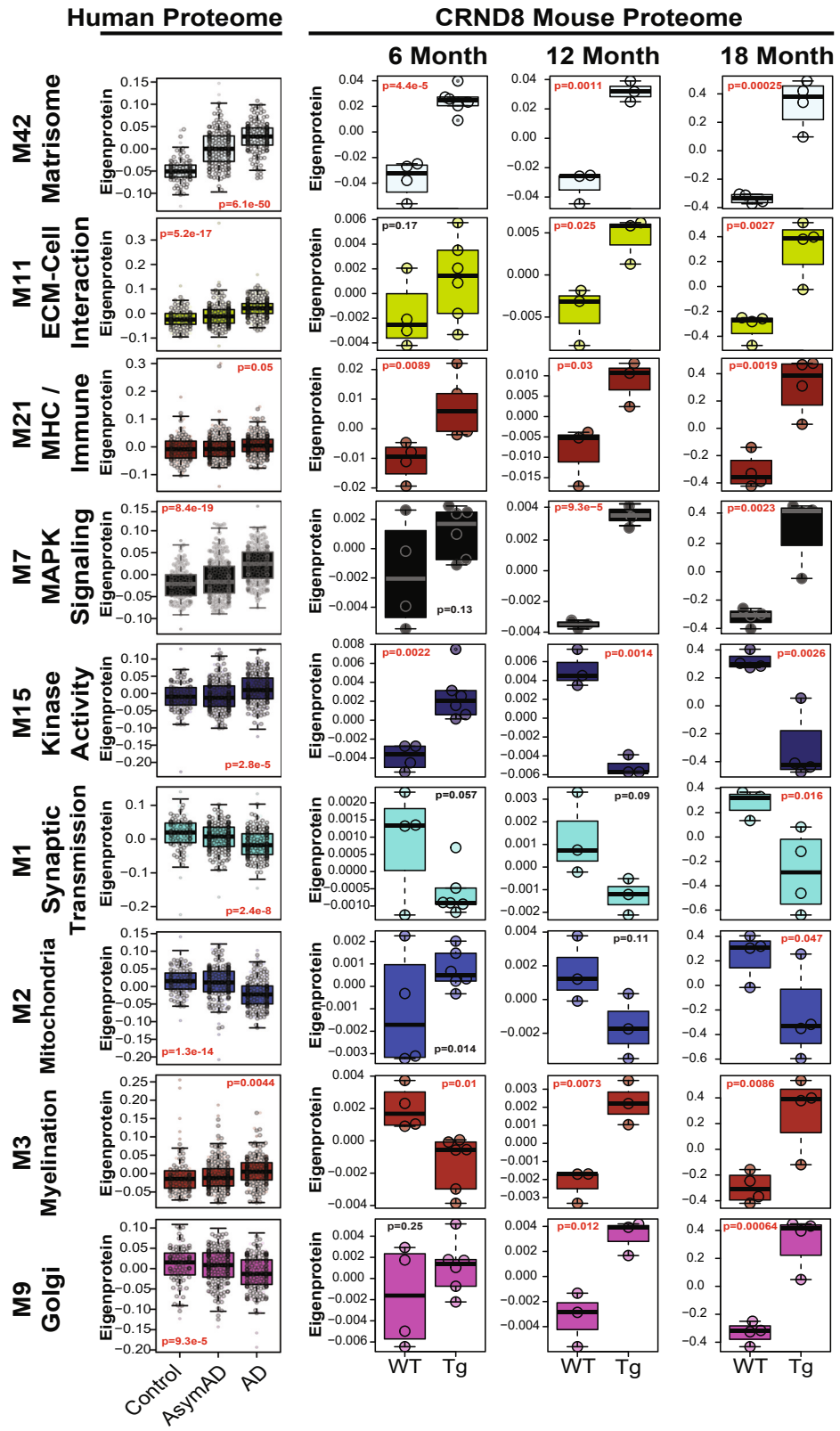

(legend on next page)

shows a decreased eigenprotein at 6M and then increased at later time points. Such data reveal complex relationships between age, pathology, and proteome changes.

Correlations between protein and RNA changes in the 18-month CRND8 brains

The overall correlation between changes in mRNA and protein levels between AD and control brains is modest.[8] We directly compared the protein and RNA levels in the 18-month CRND8 mice brains. There is a weak correlation between the changes in the common gene products detected in the 18-month CRND8 vs. non-Tg proteome at the protein and mRNA levels (Figure S2A), which is like the correlation previously observed in human brain.[8] However, when analyzed within the framework of protein modular networks, a more complex relationship between changes in mRNA levels and protein levels is observed (Figures S2B–S2D). For example, within M42, there is no correlation between protein and mRNA levels in humans and mice. However, for modules M11 and M21, there are highly significant correlations between protein and mRNA levels in the CRND8 mouse brain and human AD brain.

Validation of the proteome changes—focus on M42

We have taken a multifaceted approach to validate protein changes observed with a primary focus on M42 proteins. We also included studies of additional DEPs identified only in the CRND8 proteomes based on biological inference. We refer to this group of proteins as M42+. Several additional DEPs, which showed a log2FC > 1 in the 18-month cohort (Ctss, S100a6, and Rev3l), were also targeted in this validation even with no obvious links to M42 biology. There was a manifold rationale for the focus on M42+ proteins: it is strongly associated with core pathological features of AD and cognitive decline, APOE and APP/Aβ are present in the network, and it is the most conserved module between human AD and CRND8 mice with the largest log2FC changes not well reflected by the corresponding RNA.

MDK and PTN co-accumulate with Aβ in plaques and CAA

We focused initial studies at the brain tissue level and highlighted studies of Mdk and Ptn. Mdk and Ptn are homologous small secreted signaling molecules known to interact with heparan sulfate/heparan sulfate proteoglycans (HS/HSPGs) and signal through a set of overlapping receptors.[36,37] Mdk is significantly increased in all three cohorts studied (log2FC) with the largest log2FC of any DEP in the 6-month cohort, whereas Ptn shows significant increases in the 12 and 18-month cohorts. Select Mdk/Ptn receptors (e.g., Sdc4) are also altered at the protein level in human AD, CRND8, or both (Table S1).

Immunostaining for Mdk or Ptn shows overlap with Aβ in CRND8 mice (Figure 4A) and in the human brain (Figure 4B). Mdk and Ptn co-localize to plaques (Figure 4A) and Aβ amyloid in blood vessels associated with CAA, which is easily observed in meningeal vessels of the cerebellum (Figure 4A). In humans, both are detected in plaques and CAA deposits (Figure 4B). Mdk is more prominent in the center of the plaque in mice with the intensity of staining decreasing toward the plaque periphery (Figures 4C and 4D). Ptn staining is almost the mirror image of Mdk. In humans, MDK is more intensely detected in the plaque center, and PTN diffusely stains the fibrillar plaque (Figure 4B). In CAA, both Ptn and Mdk non-homogenously label amyloid deposits (Figure 4D). Mdk and Ptn co-localize with plaques from 3 to 12-month in CRND8 mice and with plaques in numerous lines of APP Tg mice, including mice that express Aβ42 independently of the APP[38] (Figure S3A).

Western blot analysis of 8M urea extracts from 20-month CRND8 mice brains shows an almost qualitative accumulation of both Mdk and Ptn (Figure S3B). As a characteristic feature of Aβ amyloid is the lack of solubility by strong detergent extraction, we examined solubility profiles of Mdk and Ptn in CRND8 Tg brains (Figure S3C). Low levels of Mdk and Ptn are detected in TBS and RIPA extracts, with the highest levels in the 2% SDS fraction and none detected in the 2% SDS insoluble urea-soluble fraction. The relative proportion of Mdk or Ptn appearing in each extraction was similar in the CRND8 Tg and non-Tg brains suggesting that they are not undergoing an amyloid-like structural change typically associated with detergent insolubility.[39]

Validation of additional M42+ DEP changes

Few commercially available antibodies to M42+ proteins worked in paraffin-embedded tissues; therefore, we generated and validated many new antibodies (Tables S10, S11, and S12; Figure S7A). Many antibodies to M42+ proteins stain amyloid plaques in CRND8 mice (Figure 5A; for non-Tg controls, see Figure S4). An interesting feature of these studies is that the localization of the proteins with the plaques is often morphologically distinct. For example, Slit2, Vtn, Olfml3, and others are localized within the plaque center, as observed for Mdk. Col25a1 and Dmp1 appear in more peripheral regions of the fibrillar plaque, akin to Ptn. Others show more diffuse homogenous staining of plaques (e.g., Vtn, Sdc4, and S100a6). Still, others show a patchy, nonhomogenous staining of plaques (e.g., Hgf, Spock1, ApoD, and Egfl8), which may be attributable to staining of dystrophic structures around or within the plaque. Notably, we find fixation conditions can dramatically impact the staining pattern observed, and the effects of fixation are antibody dependent (Figure S5A). Dual-labeling studies with Aβ or Thio S with a subset of these proteins reinforce the different locations within the plaque (Figure S5B). Finally, except for Mdk,

Figure 3. Select consensus human AD brain synthetic module eigenproteins show age-dependent changes in the CRND8 Tg mice

Nine consensus human modules are shown for the network of healthy control, pathology-bearing asymptomatic AD (AsymAD), and symptomatic AD (AD) individuals totaling $N = 488$ (*left panels*). To the right, the mouse orthologs of hub proteins for these modules were used to calculate the first principal component of variance in the 6, 12, and 18-month mouse proteomes, allowing for extrapolation of the modules into Tg and non-Tg mice, determination of effect size by module in each mouse cohort, and the significance of Tg effect within each module. Significant one-way ANOVA p values are colored red. Note the y axis is different across ages, and in many modules, the eigenprotein change between Tg and non-Tg mice increases dramatically with age. Visualization of all 44 modules translated to the first principal component of variance in mouse time points is available online, as described in STAR Methods and on synapse.org.[35]

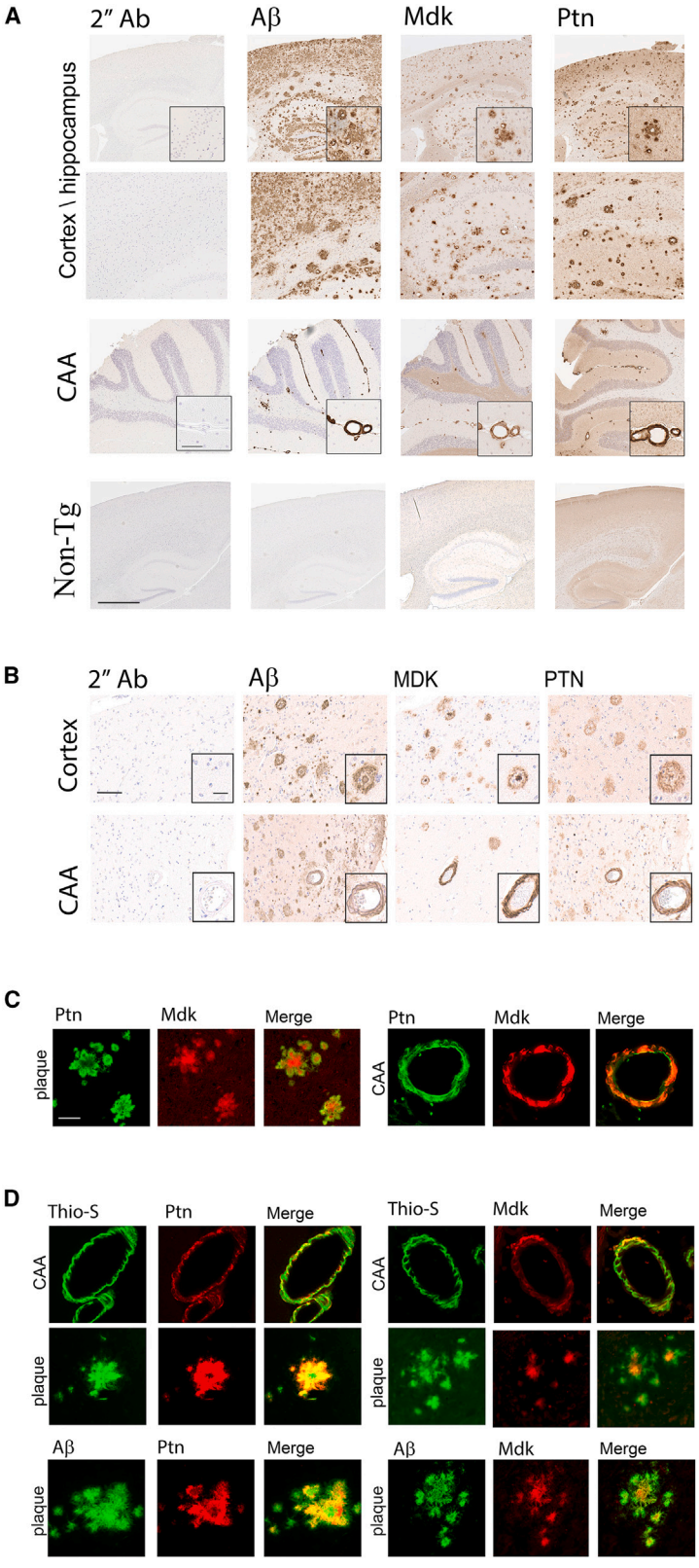

Figure 4. Mdk/MDK and Ptn/PTN colocalize with Aβ in amyloid plaques and CAA in CRND8 mice and human AD

(A) Paraffin slides containing brain tissue from 15 to 18-month CRND8 mice were stained with mouse anti-pan-Aβ, sheep anti-Mdk, or rabbit anti-Ptn antibodies. Representative low-magnification images from cortex and hippocampus (scale 500 μm) and high-magnification images (inset, scale 50 μm) were taken from cortex (plaques) and cerebellum (CAA). Non-transgenic (ntg) littermates were used as background controls.

(B) Representative low magnification (scale 100 μm) and high magnification (inset, scale 30 μm) of postmortem paraffin-embedded tissue sections of high AD human frontal cortex from a patient with high AD neuropathological changes stained for MDK and PTN.

(C) Plaques and CAA on paraffin slides containing brain tissue from old CRND8 mice were stained with anti-Mdk and anti-Ptn antibodies and visualized with fluorescent secondary antibodies (anti-rabbit green and anti-sheep red), scale 50 μm.

(D) Plaques and CAA on paraffin slides containing brain tissue from old CRND8 mice were stained with anti-pan-Aβ, anti-Mdk, or anti-Ptn antibodies and visualized with Thio-S (green) or fluorescent secondary antibodies (anti-mouse red, anti-rabbit red, and anti-sheep red), scale 50 μm.

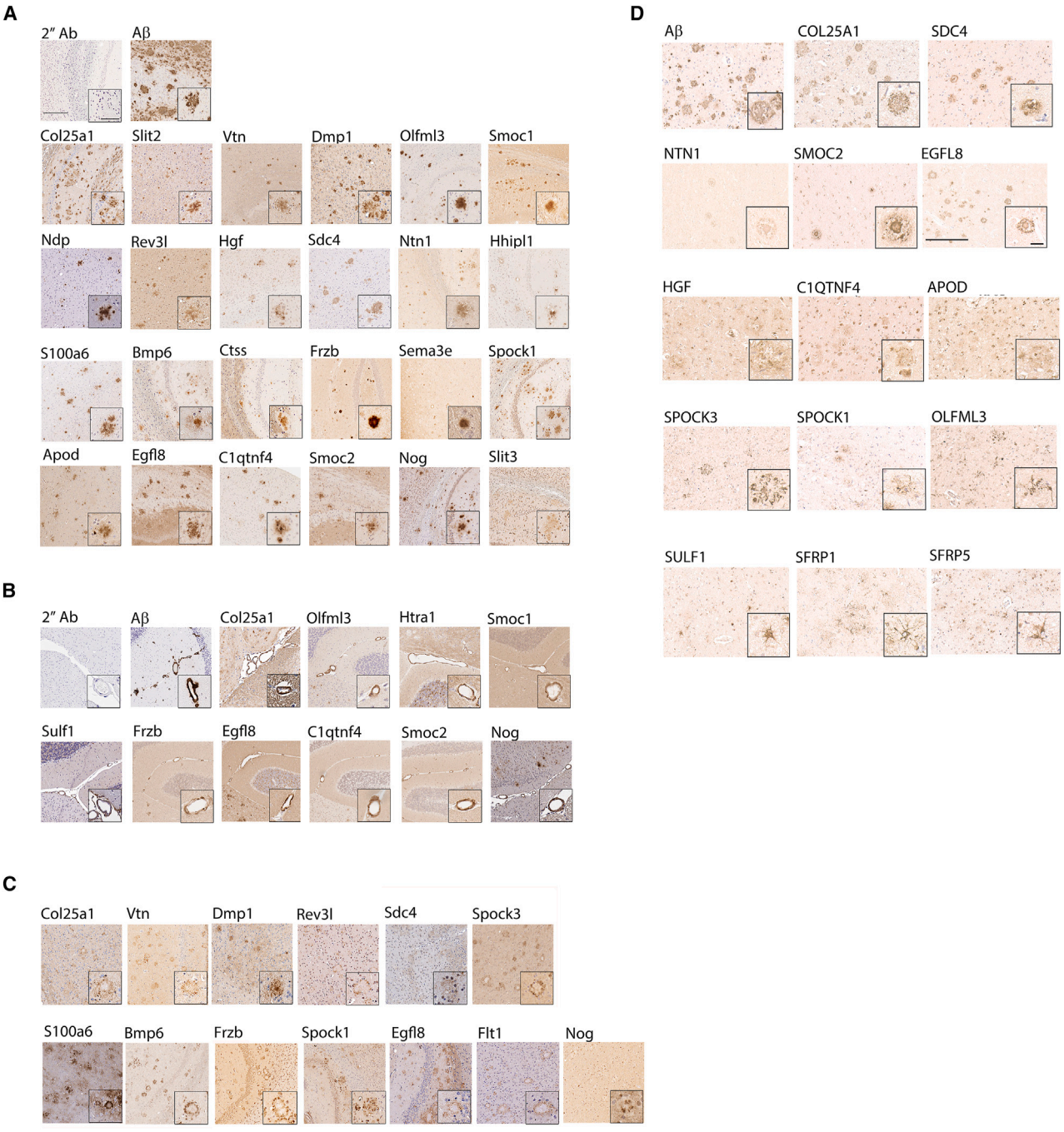

Figure 5. M42+ DEPs colocalize with amyloid pathology

Brain tissue from 15 to 18-month CRND8 mice was stained with the anti-sera against the indicated proteins. Anti-pan-Aβ antibody served as a reference for amyloid pathology, and secondary antibody alone—as a negative control. All proteins are listed in order of log2FC (highest to lowest). Representative low-magnification (scale 200 μm) and high-magnification (inset, scale 50 μm) images. See Figure S7 for non-Tg staining.

(A) DEPs in amyloid plaques in the CRND8 cortex.

(B) DEPs detected in CAA in the cerebellum.

(C) DEPs detected in dystrophic processes surrounding amyloid plaques in the cortex.

(D) Representative low magnification (scale 100 μm) and high magnification (inset, scale 30 μm) of postmortem paraffin-embedded tissue sections of high AD human frontal cortex from patients with high AD neuropathological changes stained for Aβ, EGFL8, C1QTNF4, COL25A1, HGF, APOD, SDC4, NTN1, SMOC2, OLFML3, SPOCK3, SPOCK1, SULF1, SFRP5, and SFRP1. There is selective staining of plaques by antisera for COL25A1, SDC4, NTN1, SMOC2, and EGFL8. Weaker staining of plaques and cellular staining is observed for HGF, C1QTNF4, and APOD. Dystrophic processes are stained with anti-serum to SPOCK3, SPOCK1, and OLFML3. Glial cells are detected with anti-sera to SULF1, SRRP5, and SFRP1.

Col25a1, and Ptn, which stain most plaques, most M42+ proteins are only detected in a subset of plaques (Figure 5A). In Figure 5B, we show the subset of antibodies that stain CAA in the CRND8 cerebellum. A smaller group of the M42+ DEPs is detected in CAA (Col25a1, Olfml3, Htra1, Smoc1, Sulf1, Frzb, Egfl8, C1qtnf4, Smoc2, and Nog); all co-localize with Thio S staining in the vessels (Figure S5B). Several M42 CRND8 DEPs show staining adjacent to the fibrillar plaque (Figure 5C). Spock3, Bmp6, Frzb, and Nog show staining patterns highly consistent with the classic dystrophic neurites (DNs). In contrast, Col25a1, Vtn, Rev3l, Sdc4, S100a6, Egfl8, Spock1, and Flt1 show peri-plaque staining distinct from the classic DN pattern. Selective staining of reactive astrocytes is noted for Htra1, Sulf1, Sfrp1, Hhlpl1, Spock3, Sema3d, and Smoc2 (Figure S5C).

We localized a smaller subset of the M42 proteins in AD postmortem brain tissue (Figure 5D). EGFL8, C1QTNF4, COL25A1, HGF, SDC4, NTN1, and SMOC2 all show staining in plaques. EGFL8 was not detected in the TMT-MS studies in the human brain but was detected as a DEP in CRND8 mice. OLFM3, SPOCK3, and SPOCK1 show staining of dystrophic structures around plaques. SULF1, SFRP5, and SFRP1 stain reactive astrocytes. For additional quantification of DEP accumulation during the progression of AD neuropathological changes (ADNCs), we stained frontal cortex sections of a previously published cohort of cases with low, intermediate, and high ADNCs[40] with antibodies for select DEPs and quantified the pathology burden (Figure S6A). Frontal cortex Aβ burden increases with the progression of ADNC from low to high, following the progression of diffuse plaques in this patient cohort.[40] Most proteins tested (MDK, PTN, EGFL8, and SCD4) follow a similar trajectory with increased area covered from low over intermediate to high ADNC. COL25A1 and SPOCK3, however, showed a significant increase in area covered only in high ADNC cases, following the trajectory of neuritic plaques we had recently reported for this cohort. Control brains had no detectable plaque staining (Figure S6B).

In Table S9, we compiled the staining patterns observed and annotated our findings versus previous studies in the field. We also classified the cell type expression observed for the proteins detected in these studies using data from the Allen brain atlas.[41] The extended M42+ members arise from multiple cell types representing all major brain cell types, and many mRNAs encoding these proteins are expressed at low levels (<5 Fpkm). Further, within the M42 module, only Olfml3, selectively expressed by microglia, shows a significant increase in mRNA levels in the 18-month RNA sequencing (RNA-seq) data, a finding consistent with previous RNA-seq studies of CRND8 mice brains.[34] In addition to these studies and data on Mdk and Ptn, we can also demonstrate increases in the brains of older CRND8 mice of Vtn, Htra1, Smoc1, Frzb, ApoD, and Nog by western blot analysis (Figure S7B).

Mdk or PTN overexpression both increases parenchymal amyloid and CAA in CRND8 mice and accelerates amyloid aggregation *in vivo*

We evaluated the impact of rAAV-mediated overexpression of Mdk or PTN on amyloid deposition in CRND8 mice. An initial study examined P0 ICV injections of rAAV2/8 vectors encoding Mdk or PTN after 3-month, the second at 6-month. In both cohorts, similar effects are observed; we primarily describe the 6-month analysis here (Figures 6A–6C) with the 3-month data presented in Figures S9A–S9C. Widespread overexpression of Mdk and PTN is detectable in the brain; even in small early compact plaques in the 3-month cohort, Mdk and PTN staining is observed (Figure S8A). Mdk and PTN overexpression increased parenchymal plaques (Figure 6A) and CAA (Figures 6B and S8B) and increased Aβ levels in SDS and formic acid fractions, but not in the RIPA fractions (Figures 6C and S8C), with post hoc analyses not revealing any impact of sex. These studies establish that overexpression of Mdk or PTN increases Aβ amyloid in fibrillar plaques and CAA. In the 6-month cohort, we also evaluated reactive gliosis (Figures S8D and S8E). Both Mdk and PTN increased astrocytosis and PTN increased microgliosis. We also assessed the impact of recombinant PTN and MDK on amyloid aggregation *in vitro* using standard thioflavin T (ThT) fluorescence assays (Figure 6D). PTN and MDK significantly accelerated Aβ42 aggregation at low stoichiometric molar ratios. End of assay ThT fluorescence was also increased, except for the Aβ40 PTN study, suggesting increased β sheet formation.

Select M42+ proteins bind to Aβ fibrils and a non-human, non-homologous amyloid

Many M42 proteins are known to be HS/HSPG-binding proteins. As expected, Mdk and Ptn bind immobilized heparin (Figure S9). Here, we evaluated a larger number of M42+ proteins for the potential to interact with Aβ42 fibrils and an amyloid formed from an adenovirus shaft peptide (AVS fibrils),[42,43] using a simple amyloid pull-down assay to evaluate interactions with insoluble amyloids.[44–46] As most M42+ proteins contain intrachain disulfide bonds and other post-translational modifications, these proteins were expressed in the conditioned media (CM) of HEK293 cells. Aβ42 fibrils or the AVS fibrils were then incubated with the CM and spun down to evaluate potential interactions. For the subset of proteins that we were able to detect in the media, we find that ApoE4, Mdk, Vtn, Ptn, Olfml3, Htra1, Smoc1, Sulf1, Frzb, ApoD, C1qTnf4, Smoc2, and Nog bind both Aβ42 and AVS amyloids (Figure 7A). Sfrp1 is a notable exception as it only bound Aβ fibrils in this assay.

PTN and MDK are colocalized with TTR amyloid in the human heart

The amyloid pull-down assay shows that multiple M42 proteins can interact with a generic amyloid structure. We extended this observation by evaluating whether they may accumulate in other human amyloid diseases. For these studies, we focused on *in situ* detection of MDK and PTN. As shown in Figure 7B, we find that both MDK and PTN co-localize with TTR amyloid in the heart (the third most prominent human amyloid disease).[47] A series of additional TTR cardiac amyloid cases show consistent co-localization of PTN and CLU and more variable co-localization of MDK with the TTR amyloid fibrils (Figure S10).

DEPs in CRND8 mice in the context of AD genetic studies

Previous transcriptomic studies of APP mice brains reported that highly upregulated DEGs are enriched for genes under AD

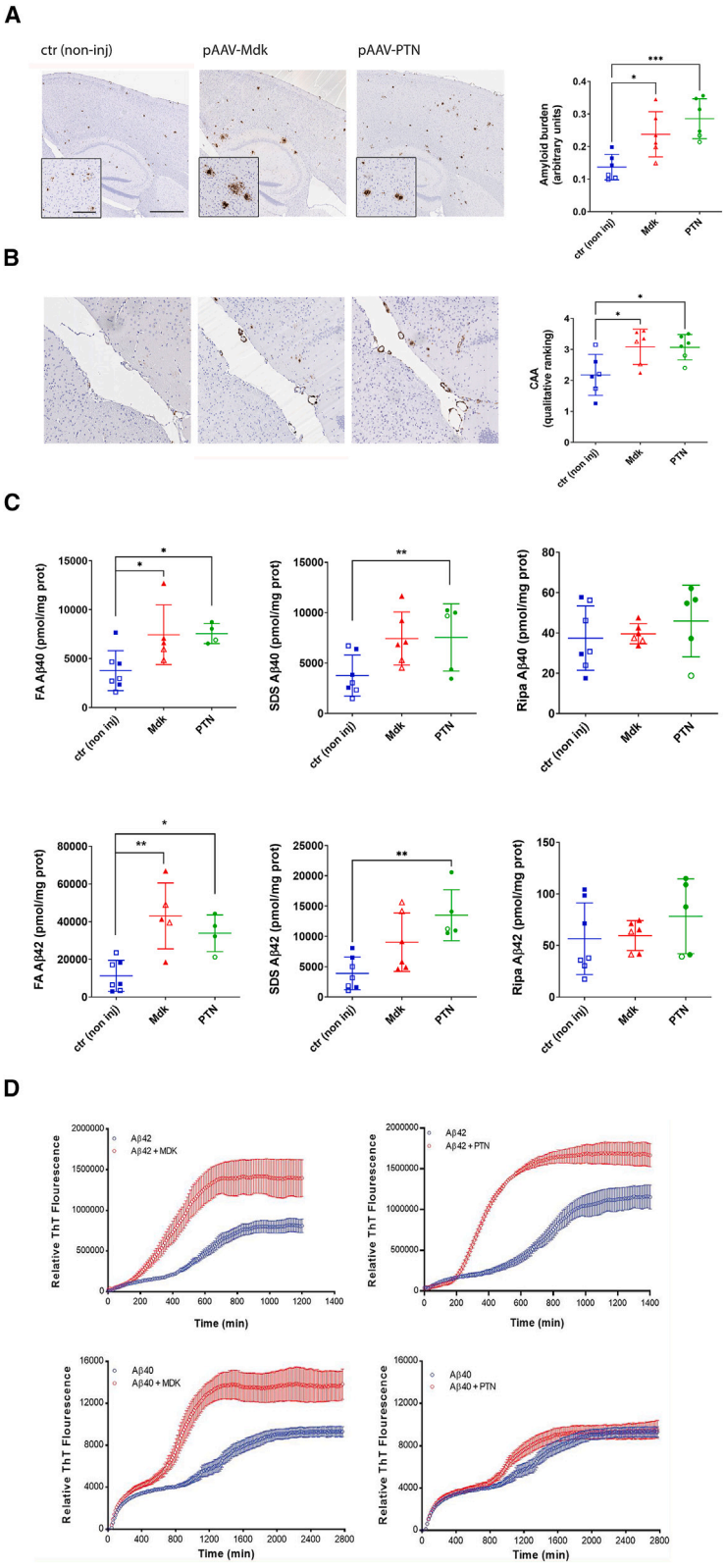

Figure 6. Mdk and PTN overexpression increase parenchymal Aβ amyloid deposition and CAA in 6-month CRND8 mice

Mice were intracerebrally injected with rAAV2/8-Mdk, rAAV2/8-PTN, or not injected (control) at P0 and aged 6 months.

(A and B) Representative images of cortex and hippocampus (A) or CAA (B) stained with biotinylated anti-Aβ mAb 33.1.1 (anti-Aβ 1–16). Scale bar: 500 μm, 50 μm (inset). Quantification data of the entire brain plaque count in three non-consecutive sections represented by a scatter dot plot of male (closed circle/square) and female (open circle/square) ± standard error of the mean. $n = 5–15$. Statistical analyses by one-way ANOVA test (*, $p < 0.05$; ***, $p < 0.001$).

(C) RIPA, 2% SDS, and 70% formic acid (FA) extracted Aβ42 and Aβ40 levels were detected by ELISA and plotted as scatter dot plot of male (closed circle/square) and female (open circle/square) ± standard error of the mean. $n = 5–12$. Aβ42 and Aβ40 levels were quantified with corresponding one-way ANOVA and paired comparison test (*, $p < 0.05$; **, $p < 0.01$, ***, $p < 0.001$).

(D) MDK and PTN accelerate amyloid aggregation *in vitro* as detected by real-time thioflavin T (ThT) assay.

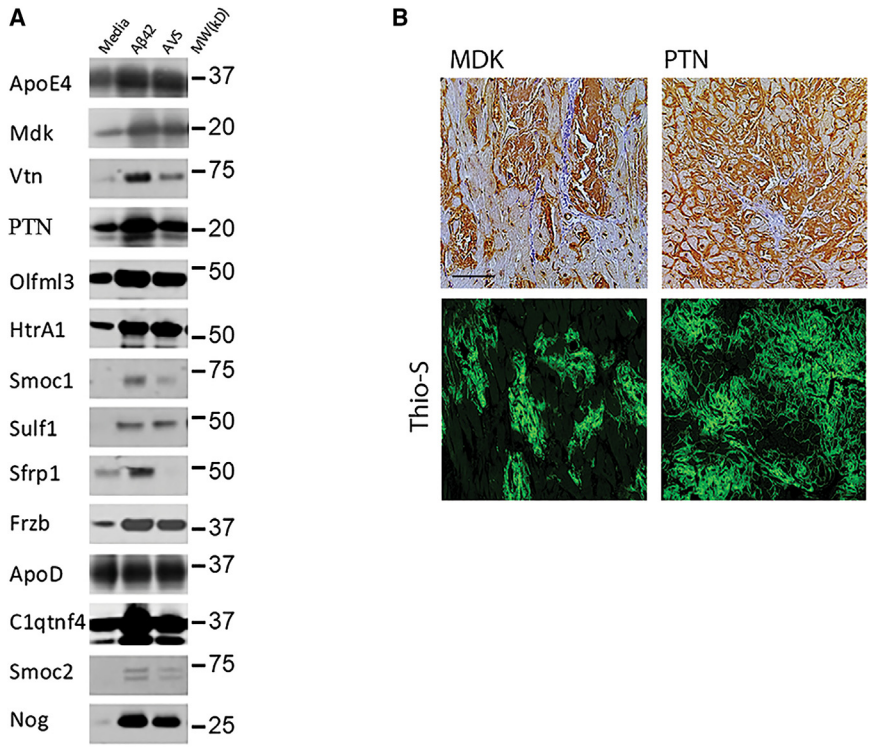

Figure 7. Amyloid binding and co-localization in TTR amyloids

(A) M42+ proteins secreted into the media of transfected HEK cells bind to Aβ42 and AVS amyloids. Data are representative of three independent experiments.

(B) Representative images of immunohistochemical stains for MDK, PTN, or Thio-S on human cardiac amyloidosis sections. Scale bar, 50 μm.

genome-wide association study (GWAS) loci or known genetic risk factors for AD.[48] We integrated data from three previous GWASs of AD to evaluate whether DEPs in CRND8 mice reflect some aspects of the genetic architecture of human AD (Table S1; Figure S11A).[49–51] Integration of the 18-month CRND8 TMT-MS data with these AD genetic studies shows that many established AD risk genes and prioritized GWAS loci (e.g., *APOE*, *BIN1*, *TREM2*, *CLU*, *SORL1*, *ACE*, *ADAM17*, *SORT1*, and *INPP5D*) are DEPs in CRND8 mice. Abca1, recently implicated as a genetic risk factor for AD, is also a DEP.[52] Notably, multiple M42+ proteins besides APOE show nominal significance in the GWASs including *COL25A1*, *SMOC1*, *HTRA1*, *DMP1*, *MDK*, *SDC4*, *SPOCK2*, *NXPH1*, and *C1QTNF4*, the latter of which lies in the *CELF1* locus and shows the highest *p* value of M42 members for AD association. Finally, we note that Grn, Sppl2a, Tmem106b, and Notch3 are all DEPs in the CRND8 proteome. *GRN* and *TMEM106B* are genetically associated with FTD-GRN, and SPPL2A is known to cleave TMEM106B potentially linking it to the biology of FTD-GRN.[53,54] Further, *NOTCH3* mutations are associated with cerebral autosomal-dominant arteriopathy with subcortical infarcts and leukoencephalopathy (CADASIL).[55] Given debate over genetic pleiotropy or inclusion of non-AD dementia in the GWASs,[56,57] these data suggest there are plausible biological links between proteins implicated in FTD and CADASIL and AD amyloid pathology.

DEPs in CRND8 mice in the context of AD CSF biomarker studies

We also evaluated the CRND8 DEPs in the context of human AD cerebrospinal fluid (CSF) biomarker studies. For this integration, we chose a dataset in which AD and control CSF were compared using a highly similar proteomic pipeline for both data generation and analysis.[58] These data show significant overlaps with other large-scale proteomic analyses of AD CSF.[58–68] Of the 1,839 in the human CSF proteomes, 257 of these are significantly altered, and of these, 62 are significantly changed in the 18-month CRND8 mice brains. 39 of these changes are congruent in directionality between the mouse brain and human CSF and 23 are discordant in directionality (Figure S11B; Table S13). Notably, 29 of the 18-month DEPs are significantly altered in the same direction in the human AD brain as in the mouse model, irrespective of the direction of change in CSF. Overall, these data support a hypothesis that select protein changes in human CSF may reflect changes in the brain related to amyloid.

DISCUSSION

Integrating newly generated deep proteomic data from CRND8 mice brains with large-scale proteomic data from human AD brain, we define an extensive Aβ/Aβ amyloid "responsome" conserved between two mouse models of Aβ deposition and human AD.[8,9,26–28] Select DEPs and protein modules show increased age dependence in magnitude of change as more Aβ amyloid accumulates, a progression observed when comparing AsymAD to AD. DEPs and overall protein changes are concordant between mouse and human in some modules but not others, reinforcing the concept that APP Tg mice are incomplete AD models.[8,9,34] Thus, we establish a paradigm for contextualizing proteomic changes that occur in human AD and provide insights into how well a model system reflects the proteomic changes in the human AD brain. These data suggest that a comparative omics network approach can provide a less biased insight into what makes a good disease model.[69,70]

CRND8 mice do not show overt neuronal loss.[24] The finding that numerous modules relating to neuronal and synaptic function (M1, M4, M5, M22, and M33) show conservation is intriguing. Numerous APP models, including CRND8 mice, have been shown to have synaptic alterations,[71–73] and in many cases, these alterations occur at early ages.[69,74,75] Neuritin and small glutamine-rich tetratricopeptide repeat-containing protein β, implicated in cognitive resilience to AD pathologies, are both consistently downregulated DEPs in the older CRND8

cohorts.[76,77] Nevertheless, these mouse models do not progress to an overt neurodegenerative state and lack neurofibrillary tangles (NFTs). Future studies contextualizing additional protein networks will deepen our understanding of the proteomic changes in mouse models that mimic human AD with additional proteomic studies on tau mice possibly identifying modules related to NFT pathology. We should consider that discordant modules in mice, such as M9 (Golgi), might serve protective functions that could alter the appearance of downstream pathologies and overt neurodegeneration in the models.[78,79]

Building deep TMT-MS proteome from the human AD brain required hundreds of samples[8,9]; in contrast, using small cohorts of CRND8 or 5XFAD mice, we can generate highly reproducible data.[13,33] From a translational point of view, these data suggest that preclinical studies in amyloid deposition models should more routinely be evaluated using systems-level proteomics including assessments of how a given intervention impacts the proteome in older mice with extensive amyloid deposition given these mice appear to better reflect the human AD proteome.

Previous studies established that several M42 proteins accumulate in amyloid plaques.[80–84] Here, we provide additional evidence that many additional M42 module proteins are present in plaques. A subset of these proteins is found in CAA, others in dystrophic processes around plaques, and others in reactive astrocytes. These studies broadly serve as a strong affirmation of the power of WGCNA to inform the pathobiology of a complex disease.[85] Indeed, these validation studies highlight the direct links between module M42 and amyloid pathology.[8,9]

Nuanced data emerging from these validation studies relate to the unique patterns of localization of these proteins within plaques and CAA. Such data along with data showing that only a subset of parenchymal plaque-associated proteins is detected in CAA raise questions about the differences between CAA and plaque amyloid and the heterogeneity of proteins within individual fibrillar plaques. Direct studies of the human CAA proteome have also found increased levels of OLFML3, PTN, and HTR1A, along with other known CAA components (e.g., APOE, CLU, and APCS).[86–88] CAA and CADASIL vessels' proteomes show overlap with each other and broad overlap with many M42+ DEPs.[86,89] Sequestration of HTRA1 with NOTCH3 in CADASIL has been proposed to lead HTRA1 loss of function and accumulation of HTRA1 substrates,[86,89] possibly mechanistically linking CADASIL to its autosomal recessive phenocopy cerebral autosomal recessive arteriopathy with subcortical infarcts and leukoencephalopathy, which is caused by heterozygous loss of function mutations in *HTRA1*. By inference, these data showing Htra1 in CAA have mechanistic implications for CAA-driven vascular dysfunction in AD.

Overexpression studies of Mdk or PTN in the CRND8 brain result in increased CAA and parenchymal Aβ amyloid, demonstrating these proteins have a direct impact on amyloid deposition and represent novel therapeutic targets in AD. As both proteins accelerate aggregation of Aβ and bind preexisting amyloid fibrils *in vitro*, we hypothesize they act as amyloid chaperones likely directly impacting the rate of Aβ aggregation. However, Mdk also impacts myeloid cells, and its co-accumulation in plaques could impact microglial-mediated clearance either through gain or loss of function.[90,91] Ptn, which signals through the same receptors as Mdk, could have similar impacts.[92] Thus, these proteins may also influence cell-mediated clearance of Aβ. Additional studies will be needed to evaluate the impact of Mdk and Ptn and the many co-accumulating proteins on amyloid deposition and peri-plaque cellular responses. Though a previous study had claimed that a Mdk knockout crossed into an APP Tg line resulted in increased amyloid, these data are anecdotal and not rigorous.[93] Non-Tg mice Mdk and Ptn knockouts were also studied and claimed to increase amyloid deposition, but in that study, an antibody selective for human Aβ was used to stain "plaques"; these results are likely artifactual.

HS and HSPGs and chondroitin sulfate proteoglycans (CSPGs) have been implicated in the biology of AD and other amyloid deposits.[94] HS and select HSPG core proteins (e.g., HSPG2 and ACAN) accumulate in plaques and DNs. Select HSPGs also accelerate Aβ aggregation and mediate the internalization of extracellular tau.[95] Though we detect HSPG2, ACAN, and CSPGs, they are minimally altered (Table S1). In contrast, in human AD, the HSPGs, GPC4, 5, SPOCK1–3, and SDC2, 4 are much more robust DEPs and several are also core M42 module members. In CRND8 mice, Gpc1, 5, Spock1–3, and Sdc2, 4 are also robust DEPs (Table S1).

Most M42+ proteins assayed here bind Aβ42 amyloid and non-human, non-homologous amyloid fibrils.[42,43] These data led us to explore whether MDK and PTN might be components of peripheral amyloids and both accumulate in TTR cardiac amyloid. Neither has been previously detected, even in laser-capture proteomic studies of cardiac amyloid deposits.[96] As HS/HSPGs are common components of human amyloids, these studies suggest that there may be very complex multipartite structural interactions between amyloid, HS/HSPGs, and these co-accumulating proteins.

Given intensive studies of both Aβ amyloid and peripheral amyloids, it is somewhat surprising that we and others are documenting additional proteins co-accumulating with amyloid.[13,32,33,96,97] In our studies, brain tissue was extracted with 8M urea; thus, we are studying the total detectable urea-solubilized proteome and not the detergent-insoluble proteome. Indeed, for Mdk and Ptn in mice brains, we find no gross change in solubility, despite the large increase in the Tg mouse brains. These initial solubility studies likely explain why many of these proteins are not detected in detergent-insoluble fractions typically used to isolate amyloid; they simply may not be there.

Our current data and data from others reveal numerous proteins that co-deposit with Aβ amyloid. Further, given the large number of proteins showing age-progressive increases in the CRND8 mice brain, it is highly likely that over time many additional proteins will be found to accumulate with Aβ amyloid or in cellular processes around plaques and in other amyloid diseases. Two recently identified components of Aβ plaques, Pycard and Mfge8, are increased DEPs in our data, but in 18-month CRND8, they rank 296th and 300th among all the increased DEPs in terms of log2FC.[98,99] In the human AD proteome, PYCARD is significantly increased (log2FC = 0.06), and MFGE8 is detected but not increased.

There is ongoing debate as to how amyloid or Aβ aggregate pathology drives cellular dysfunction and degeneration in AD.[2,6,7] More generally, this debate extends to all amyloid

disorders and how amyloid accumulation causes tissue damage and organ dysfunction.[39,47,100] Indeed, extensive efforts have been made to identify toxic species or conformers.[101] Our current data and previous studies of proteins that co-accumulate with amyloid offer an alternative hypothesis to the concept that amyloid or amyloid-like aggregate is directly toxic.[75,102] We term this the "amyloid scaffold" hypothesis (Figure S12) and posit that if amyloid deposits scaffold the accumulation of numerous proteins, then perhaps the accumulation of these proteins mediates downstream pathophysiology. Many of the proteins detected in plaques and CAA are known signaling molecules, and their accumulation could impact dystrophic neurite and reactive glia in the local plaque microenvironment or cells in the vessel wall. Accumulation of proteins within amyloid deposits could lead to a gain of normal function, if these proteins retain activity. Such binding may also activate novel signaling pathways. Sequestration could also result in loss of function and reduced levels in the surrounding tissue. In the heart, MDK can promote intimal hyperplasia whereas PTN has been shown to have angiogenic effects.[103–105] Thus, this hypothesis may have relevance for peripheral amyloidoses as well. There are also intriguing parallels between this concept of amyloid as a scaffold in disease and functional amyloids, which have been proposed to mediate biological effects in part through a scaffolding mechanism (reviewed in the study by Rubel et al.[106]).

It is important to consider that the accumulation of proteins in the plaque is not simply a bystander effect, but part of the response to amyloid as a danger-associated molecular pattern.[107,108] The amyloid "scaffold" and amyloid (or oligomer) as "direct toxin" hypotheses are not mutually exclusive.[34,75] Many proteins that interact with amyloid may be involved in clearance, coating, and neutralization of the structure to reduce toxicity, or some combination of these. Other components may simply be bystanders, at least concerning impacts on amyloid deposition, but once present, they could still mediate pathology by altering signaling gradients.

There is extensive data that APOE and CLU interaction with Aβ/Aβ amyloid deposits alters the local cellular response and influences amyloid deposition.[80–82,109,110] Because of their genetic association with AD, they are also considered therapeutic targets.[111] We have not yet explored studies in knockout mice; however, overexpression studies suggest that Mdk and PTN, like APOE and CLU, can increase amyloid deposition and both also increase CAA. Thus, like APOE and CLU, they represent possibly therapeutic targets. It will be intriguing to evaluate the impacts of the larger set of proteins that are now being shown to co-accumulate. We speculate that some will promote amyloid deposition, others block it, and still others simply bind without altering deposition. Additional probes of M42+ proteins' biology will be necessary to determine their role in AD and their druggability.

Integrating data from genetic studies of AD and CSF biomarkers reinforces links between many established AD genes or prioritized genetic loci and AD risk genes and regulation of Aβ catabolism and deposition or response to Aβ deposition and suggests that select CSF biomarkers might reflect the impacts of amyloid pathology in AD. Recently, SMOC1 and SPON1, two core M42 members, are altered in concert with decreases in Aβ42/40 ratios in the CSF of individuals with dominantly inherited AD.[63] Further, Smoc1 is a highly reproducible, highly upregulated AD CSF biomarker.[59,63,67,112]

In summary, this contextualized understanding of AD and APP mouse model proteomic changes provides insights into the molecular complexity of AD pathogenesis and informs biomarkers and novel therapeutic targets related to amyloid deposition. Though we have (1) validated some of the more robust protein changes in the proteomic analyses, (2) provided pathological insight related to a subset of these proteins, and (3) generated initial modeling and biochemical data to support potential pathobiological roles, there is still much to be learned about amyloid and its role in AD pathophysiology and other amyloid disorders. Future integrative omic studies can build on and refine these current studies, especially by incorporating models of additional pathologies relevant to AD and other amyloidoses.

Limitations of the study

Select overarching limitations are highlighted here. First, the pathological validation studies vary according to the confidence in the findings, as a subset of the pathological findings is based on a single antibody or antisera. Second, we do not have extensive proteomic data from human brains with amyloid deposition before the presence of other pathologies. Thus, our integration of the mouse data is limited to human brain data with a spectrum of AD pathologies. Third, the lack of analyses of a group of mice young enough to lack amyloid deposition or manipulation that alters amyloid loads imposes some interpretative limitations on the data concerning changes driven by amyloid or mutant APP overexpression. Nevertheless, given multiple layers of orthogonal and integrative data used in this study, we believe that this study begins to capture and contextualize proteomic changes in AD and mouse models of amyloid deposition to inform downstream studies.

STAR★METHODS

Detailed methods are provided in the online version of this paper and include the following:

- KEY RESOURCES TABLE
- RESOURCE AVAILABILITY
  - Lead contact
  - Materials availability
  - Data and code availability
- EXPERIMENTAL MODELS AND SUBJECT DETAILS
  - Human subjects
  - Cell lines
  - Animal models
- METHOD DETAILS
  - Cloning
  - Neonatal injections
  - Mouse brain histology and immunohistochemistry
  - Human tissue histology and immunohistochemistry
  - Quantification of area covered (human tissue)
  - Aβ ELISAs
  - Amyloid-β aggregation assay
  - Pulldowns and western blot analysis
  - Proteomic sample processing
  - Tandem mass tag (TMT) labeling
  - High pH fractionation
  - Liquid chromatography-tandem mass spectrometry
  - Proteome identification and quantification with proteome discoverer

SUPPLEMENTAL INFORMATION

Supplemental information can be found online at https://doi.org/10.1016/j.xcrm.2024.101669.

ACKNOWLEDGMENTS

This study was supported by the following National Institutes of Health (NIH) funding mechanisms: P30AG066506, U01AG061357, U01AG046139 (T.E.G. and N.E.-T.), RF1AG074569 (Y.L., S.P., and T.E.G.), RF1AG071587 (N.T.S.), and P30AG066511 (A.I.L.) and the Foundations for the National Institutes of Health AMP-AD 2.0 grant. This work was supported by the Deutsche Forschungsgemeinschaft (DFG, German Research Foundation) under Germany's Excellence Strategy NeuroCure – EXC-2049 – 390688087 to F.L.H., as well as HE 3130/6-1 to F.L.H. Additional support for these studies was provided by the NIA grants R01AG061796 (N.E.-T.) and U19AG074879 (N.E.-T.) and Alzheimer's Association Zenith Fellows Award (N.E.-T.).

AUTHOR CONTRIBUTIONS

Conceptualization, T.E.G., N.T.S., S.P., A.I.L., Y.L., E.C.B.J., and E.B.D.; methodology, T.E.G., Y.L., Y.R., D.D., J.G., N.T.S., M.A., K.D., D.R., J.T., C.M., J.P., A.I., A.E., B.D.M., K.D., A.N., T.I., F.A., T.L., K.M., S.R., B.D.M., M.R., and C.C.F.; investigation, Y.L., E.B.D., Y.R., W.T., D.D., M.A., J.G., K.L., J.T.-L., J.P., A.I., A.E., B.D.M., K.M., and A.N.; formal analysis, Y.L., K.M., E.B.D., M.R., C.C.F., N.T.S., T.E.G., and A.N.; writing – original draft, T.E.G., Y.L., and S.P.; writing – review and editing, Y.L., E.B.D., D.D., N.E.-T., J.W.K., A.I.L., K.M., N.T.S., T.E.G., S.P., and F.L.H.; funding acquisition, T.E.G., S.P., N.T.S., Y.L., and A.I.L.; resources, A.I.L., J.W.K., N.T.S., S.P., T.E.G., E.C.B.J., F.L.H., J.W.K., and J.J.; and all authors read and approved the final manuscript.

DECLARATION OF INTERESTS

The authors declare no competing interests.

Received: August 3, 2023
Revised: April 15, 2024
Accepted: July 10, 2024
Published: August 9, 2024

REFERENCES

1. Hardy, J., and Selkoe, D.J. (2002). The amyloid hypothesis of Alzheimer's disease: progress and problems on the road to therapeutics. Science *297*, 353–356.
2. Golde, T.E. (2022). Alzheimer's disease - the journey of a healthy brain into organ failure. Mol. Neurodegener. *17*, 18. https://doi.org/10.1186/s13024-022-00523-1.
3. Budd Haeberlein, S., Aisen, P.S., Barkhof, F., Chalkias, S., Chen, T., Cohen, S., Dent, G., Hansson, O., Harrison, K., von Hehn, C., et al. (2022). Two Randomized Phase 3 Studies of Aducanumab in Early Alzheimer's Disease. J. Prev. Alzheimers Dis. *9*, 197–210. https://doi.org/10.14283/jpad.2022.30.
4. Sims, J.R., Zimmer, J.A., Evans, C.D., Lu, M., Ardayfio, P., Sparks, J., Wessels, A.M., Shcherbinin, S., Wang, H., Monkul Nery, E.S., et al. (2023). Donanemab in Early Symptomatic Alzheimer Disease: The TRAILBLAZER-ALZ 2 Randomized Clinical Trial. JAMA *330*, 512–527. https://doi.org/10.1001/jama.2023.13239.
5. van Dyck, C.H., Swanson, C.J., Aisen, P., Bateman, R.J., Chen, C., Gee, M., Kanekiyo, M., Li, D., Reyderman, L., Cohen, S., et al. (2023). Lecanemab in Early Alzheimer's Disease. N. Engl. J. Med. *388*, 9–21. https://doi.org/10.1056/NEJMoa2212948.
6. Murdock, M.H., and Tsai, L.H. (2023). Insights into Alzheimer's disease from single-cell genomic approaches. Nat. Neurosci. *26*, 181–195. https://doi.org/10.1038/s41593-022-01222-2.
7. Long, J.M., and Holtzman, D.M. (2019). Alzheimer Disease: An Update on Pathobiology and Treatment Strategies. Cell *179*, 312–339. https://doi.org/10.1016/j.cell.2019.09.001.
8. Johnson, E.C.B., Carter, E.K., Dammer, E.B., Duong, D.M., Gerasimov, E.S., Liu, Y., Liu, J., Betarbet, R., Ping, L., Yin, L., et al. (2022). Large-scale deep multi-layer analysis of Alzheimer's disease brain reveals strong proteomic disease-related changes not observed at the RNA level. Nat. Neurosci. *25*, 213–225. https://doi.org/10.1038/s41593-021-00999-y.
9. Johnson, E.C.B., Dammer, E.B., Duong, D.M., Ping, L., Zhou, M., Yin, L., Higginbotham, L.A., Guajardo, A., White, B., Troncoso, J.C., et al. (2020). Large-scale proteomic analysis of Alzheimer's disease brain and cerebrospinal fluid reveals early changes in energy metabolism associated with microglia and astrocyte activation. Nat. Med. *26*, 769–780. https://doi.org/10.1038/s41591-020-0815-6.
10. Wan, Y.W., Al-Ouran, R., Mangleburg, C.G., Perumal, T.M., Lee, T.V., Allison, K., Swarup, V., Funk, C.C., Gaiteri, C., Allen, M., et al. (2020). Meta-Analysis of the Alzheimer's Disease Human Brain Transcriptome and Functional Dissection in Mouse Models. Cell Rep. *32*, 107908. https://doi.org/10.1016/j.celrep.2020.107908.
11. Allen, M., Carrasquillo, M.M., Funk, C., Heavner, B.D., Zou, F., Younkin, C.S., Burgess, J.D., Chai, H.S., Crook, J., Eddy, J.A., et al. (2016). Human whole genome genotype and transcriptome data for Alzheimer's and other neurodegenerative diseases. Sci. Data *3*, 160089. https://doi.org/10.1038/sdata.2016.89.
12. Wang, X., Allen, M., Is, O., Reddy, J.S., Tutor-New, F.Q., Castanedes Casey, M., Carrasquillo, M.M., Oatman, S.R., Min, Y., Asmann, Y.W., et al. (2021). Alzheimer's disease and progressive supranuclear palsy share similar transcriptomic changes in distinct brain regions. J. Clin. Invest. *132*, e149904. https://doi.org/10.1172/JCI149904.
13. Bai, B., Wang, X., Li, Y., Chen, P.C., Yu, K., Dey, K.K., Yarbro, J.M., Han, X., Lutz, B.M., Rao, S., et al. (2020). Deep Multilayer Brain Proteomics Identifies Molecular Networks in Alzheimer's Disease Progression. Neuron *106*, 700. https://doi.org/10.1016/j.neuron.2020.04.031.
14. Bai, B., Hales, C.M., Chen, P.C., Gozal, Y., Dammer, E.B., Fritz, J.J., Wang, X., Xia, Q., Duong, D.M., Street, C., et al. (2013). U1 small nuclear ribonucleoprotein complex and RNA splicing alterations in Alzheimer's disease. Proc. Natl. Acad. Sci. USA *110*, 16562–16567. https://doi.org/10.1073/pnas.1310249110.
15. Zhang, B., Gaiteri, C., Bodea, L.G., Wang, Z., McElwee, J., Podtelezhnikov, A.A., Zhang, C., Xie, T., Tran, L., Dobrin, R., et al. (2013). Integrated systems approach identifies genetic nodes and networks in late-onset Alzheimer's disease. Cell *153*, 707–720. https://doi.org/10.1016/j.cell.2013.03.030.
16. Rayaprolu, S., Higginbotham, L., Bagchi, P., Watson, C.M., Zhang, T., Levey, A.I., Rangaraju, S., and Seyfried, N.T. (2021). Systems-based proteomics to resolve the biology of Alzheimer's disease beyond amyloid and tau. Neuropsychopharmacology *46*, 98–115. https://doi.org/10.1038/s41386-020-00840-3.
17. Drummond, E., Kavanagh, T., Pires, G., Marta-Ariza, M., Kanshin, E., Nayak, S., Faustin, A., Berdah, V., Ueberheide, B., and Wisniewski, T. (2022). The amyloid plaque proteome in early onset Alzheimer's disease and Down syndrome. Acta Neuropathol. Commun. *10*, 53. https://doi.org/10.1186/s40478-022-01356-1.
18. De Jager, P.L., Yang, H.S., and Bennett, D.A. (2018). Deconstructing and targeting the genomic architecture of human neurodegeneration. Nat. Neurosci. *21*, 1310–1317. https://doi.org/10.1038/s41593-018-0240-z.
19. Xiong, X., James, B.T., Boix, C.A., Park, Y.P., Galani, K., Victor, M.B., Sun, N., Hou, L., Ho, L.L., Mantero, J., et al. (2023). Epigenomic

dissection of Alzheimer's disease pinpoints causal variants and reveals epigenome erosion. Cell *186*, 4422–4437.e21. https://doi.org/10.1016/j.cell.2023.08.040.

20. Sun, N., Victor, M.B., Park, Y.P., Xiong, X., Scannail, A.N., Leary, N., Prosper, S., Viswanathan, S., Luna, X., Boix, C.A., et al. (2023). Human microglial state dynamics in Alzheimer's disease progression. Cell *186*, 4386–4403.e29. https://doi.org/10.1016/j.cell.2023.08.037.
21. Sun, N., Akay, L.A., Murdock, M.H., Park, Y., Galiana-Melendez, F., Bubnys, A., Galani, K., Mathys, H., Jiang, X., Ng, A.P., et al. (2023). Single-nucleus multiregion transcriptomic analysis of brain vasculature in Alzheimer's disease. Nat. Neurosci. *26*, 970–982. https://doi.org/10.1038/s41593-023-01334-3.
22. Mathys, H., Peng, Z., Boix, C.A., Victor, M.B., Leary, N., Babu, S., Abdelhady, G., Jiang, X., Ng, A.P., Ghafari, K., et al. (2023). Single-cell atlas reveals correlates of high cognitive function, dementia, and resilience to Alzheimer's disease pathology. Cell *186*, 4365–4385.e27. https://doi.org/10.1016/j.cell.2023.08.039.
23. Wang, X., Allen, M., Li, S., Quicksall, Z.S., Patel, T.A., Carnwath, T.P., Reddy, J.S., Carrasquillo, M.M., Lincoln, S.J., Nguyen, T.T., et al. (2020). Deciphering cellular transcriptional alterations in Alzheimer's disease brains. Mol. Neurodegener. *15*, 38. https://doi.org/10.1186/s13024-020-00392-6.
24. Chishti, M.A., Yang, D.S., Janus, C., Phinney, A.L., Horne, P., Pearson, J., Strome, R., Zuker, N., Loukides, J., French, J., et al. (2001). Early-onset amyloid deposition and cognitive deficits in transgenic mice expressing a double mutant form of amyloid precursor protein 695. J. Biol. Chem. *276*, 21562–21570.
25. Oakley, H., Cole, S.L., Logan, S., Maus, E., Shao, P., Craft, J., Guillozet-Bongaarts, A., Ohno, M., Disterhoft, J., Van Eldik, L., et al. (2006). Intraneuronal beta-amyloid aggregates, neurodegeneration, and neuron loss in transgenic mice with five familial Alzheimer's disease mutations: potential factors in amyloid plaque formation. J. Neurosci. *26*, 10129–10140. https://doi.org/10.1523/JNEUROSCI.1202-06.2006.
26. Reddy, J.S., Heath, L., Linden, A.V., Allen, M., de Paiva Lopes, K., Seifar, F., Wang, E., Ma, Y., Poehlman, W.L., Quicksall, Z.S., et al. (2024). Bridging the Gap: Multi-Omics Profiling of Brain Tissue in Alzheimer's Disease and Older Controls in Multi-Ethnic Populations. bioRxiv. https://doi.org/10.1101/2024.04.16.589592.
27. Seifar, F., Fox, E.J., Shantaraman, A., Liu, E.B., Dammer, E.B., Moideste, E., Duong, D.M., Yin, L., Trautwig, A.M., Guo, Q., et al. (2024). Large-scale Deep Proteomic Analysis in Alzheimer's Disease Brain Regions Across Race and Ethnicity. bioRxiv. https://doi.org/10.1101/2024.04.22.590547.
28. Kumar, P., Goettemoeller, A.M., Espinosa-Garcia, C., Tobin, B.R., Tfaily, A., Nelson, R.S., Natu, A., Dammer, E.B., Santiago, J.V., Malepati, S., et al. (2024). Native-state proteomics of Parvalbumin interneurons identifies unique molecular signatures and vulnerabilities to early Alzheimer's pathology. Nat. Commun. *15*, 2823. https://doi.org/10.1038/s41467-024-47028-7.
29. Cao, X., and Sudhof, T.C. (2001). A transcriptionally [correction of transcriptively] active complex of APP with Fe65 and histone acetyltransferase Tip60. Science *293*, 115–120.
30. Balklava, Z., Niehage, C., Currinn, H., Mellor, L., Guscott, B., Poulin, G., Hoflack, B., and Wassmer, T. (2015). The Amyloid Precursor Protein Controls PIKfyve Function. PLoS One *10*, e0130485. https://doi.org/10.1371/journal.pone.0130485.
31. Zhang, T., Yu, J., Wang, G., and Zhang, R. (2021). Amyloid precursor protein binds with TNFRSF21 to induce neural inflammation in Alzheimer's Disease. Eur. J. Pharm. Sci. *157*, 105598. https://doi.org/10.1016/j.ejps.2020.105598.
32. Askenazi, M., Kavanagh, T., Pires, G., Ueberheide, B., Wisniewski, T., and Drummond, E. (2023). Compilation of reported protein changes in the brain in Alzheimer's disease. Nat. Commun. *14*, 4466. https://doi.org/10.1038/s41467-023-40208-x.
33. Bai, B., Vanderwall, D., Li, Y., Wang, X., Poudel, S., Wang, H., Dey, K.K., Chen, P.C., Yang, K., and Peng, J. (2021). Proteomic landscape of Alzheimer's Disease: novel insights into pathogenesis and biomarker discovery. Mol. Neurodegener. *16*, 55. https://doi.org/10.1186/s13024-021-00474-z.
34. McFarland, K.N., Ceballos, C., Rosario, A., Ladd, T., Moore, B., Golde, G., Wang, X., Allen, M., Ertekin-Taner, N., Funk, C.C., et al. (2021). Microglia show differential transcriptomic response to Aβ peptide aggregates ex vivo and in vivo. Life Sci. Alliance *4*, e202101108. https://doi.org/10.26508/lsa.202101108.
35. Dammer, E.B., Levites, Y.L.,N.T.,S., and Golde, T.E. (2024). Extended Data for Levites Y, Dammer EB. Cell Rep Med *2024*. (synpase.org).
36. Winkler, C., and Yao, S. (2014). The midkine family of growth factors: diverse roles in nervous system formation and maintenance. Br. J. Pharmacol. *171*, 905–912. https://doi.org/10.1111/bph.12462.
37. Herradon, G., and Perez-Garcia, C. (2014). Targeting midkine and pleiotrophin signalling pathways in addiction and neurodegenerative disorders: recent progress and perspectives. Br. J. Pharmacol. *171*, 837–848. https://doi.org/10.1111/bph.12312.
38. Xu, G., Fromholt, S.E., Chakrabarty, P., Zhu, F., Liu, X., Pace, M.C., Koh, J., Golde, T.E., Levites, Y., Lewis, J., and Borchelt, D.R. (2020). Diversity in Aβ deposit morphology and secondary proteome insolubility across models of Alzheimer-type amyloidosis. Acta Neuropathol. Commun. *8*, 43. https://doi.org/10.1186/s40478-020-00911-y.
39. Glenner, G.G. (1980). Amyloid deposits and amyloidosis. The beta-fibrilloses (first of two parts). N. Engl. J. Med. *302*, 1283–1292.
40. Tsering, W., Hery, G.P., Phillips, J.L., Lolo, K., Bathe, T., Villareal, J.A., Ruan, I.Y., and Prokop, S. (2023). Transformation of non-neuritic into neuritic plaques during AD progression drives cortical spread of tau pathology via regenerative failure. Acta Neuropathol. Commun. *11*, 190. https://doi.org/10.1186/s40478-023-01688-6.
41. Yao, Z., van Velthoven, C.T.J., Nguyen, T.N., Goldy, J., Sedeno-Cortes, A.E., Baftizadeh, F., Bertagnolli, D., Casper, T., Chiang, M., Crichton, K., et al. (2021). A taxonomy of transcriptomic cell types across the isocortex and hippocampal formation. Cell *184*, 3222–3241.e26. https://doi.org/10.1016/j.cell.2021.04.021.
42. Luckey, M., Hernandez, J., Arlaud, G., Forsyth, V.T., Ruigrok, R.W., and Mitraki, A. (2000). A peptide from the adenovirus fiber shaft forms amyloid-type fibrils. FEBS Lett. *468*, 23–27.
43. Papanikolopoulou, K., Schoehn, G., Forge, V., Forsyth, V.T., Riekel, C., Hernandez, J.F., Ruigrok, R.W., and Mitraki, A. (2005). Amyloid fibril formation from sequences of a natural beta-structured fibrous protein, the adenovirus fiber. J. Biol. Chem. *280*, 2481–2490.
44. Levites, Y., Jansen, K., Smithson, L.A., Dakin, R., Holloway, V.M., Das, P., and Golde, T.E. (2006). Intracranial adeno-associated virus-mediated delivery of anti-pan amyloid beta, amyloid beta40, and amyloid beta42 single-chain variable fragments attenuates plaque pathology in amyloid precursor protein mice. J. Neurosci. *26*, 11923–11928. https://doi.org/10.1523/JNEUROSCI.2795-06.2006.
45. Chakrabarty, P., Li, A., Ladd, T.B., Strickland, M.R., Koller, E.J., Burgess, J.D., Funk, C.C., Cruz, P.E., Allen, M., Yaroshenko, M., et al. (2018). TLR5 decoy receptor as a novel anti-amyloid therapeutic for Alzheimer's disease. J. Exp. Med. *215*, 2247–2264. https://doi.org/10.1084/jem.20180484.
46. Lessard, C.B., Malnik, S.L., Zhou, Y., Ladd, T.B., Cruz, P.E., Ran, Y., Mahan, T.E., Chakrabaty, P., Holtzman, D.M., Ulrich, J.D., et al. (2018). High-affinity interactions and signal transduction between Aβ oligomers and TREM2. EMBO Mol. Med. *10*, e9027. https://doi.org/10.15252/emmm.201809027.
47. Eisenberg, D., and Jucker, M. (2012). The amyloid state of proteins in human diseases. Cell *148*, 1188–1203. https://doi.org/10.1016/j.cell.2012.02.022.

48. Matarin, M., Salih, D.A., Yasvoina, M., Cummings, D.M., Guelfi, S., Liu, W., Nahaboo Solim, M.A., Moens, T.G., Paublete, R.M., Ali, S.S., et al. (2015). A genome-wide gene-expression analysis and database in transgenic mice during development of amyloid or tau pathology. Cell Rep. *10*, 633–644. https://doi.org/10.1016/j.celrep.2014.12.041.

49. Kunkle, B.W., Grenier-Boley, B., Sims, R., Bis, J.C., Damotte, V., Naj, A.C., Boland, A., Vronskaya, M., van der Lee, S.J., Amlie-Wolf, A., et al. (2019). Genetic meta-analysis of diagnosed Alzheimer's disease identifies new risk loci and implicates Aβ, tau, immunity and lipid processing. Nat. Genet. *51*, 414–430. https://doi.org/10.1038/s41588-019-0358-2.

50. Bellenguez, C., Kucukali, F., Jansen, I.E., Kleineidam, L., Moreno-Grau, S., Amin, N., Naj, A.C., Campos-Martin, R., Grenier-Boley, B., Andrade, V., et al. (2022). New insights into the genetic etiology of Alzheimer's disease and related dementias. Nat. Genet. *54*, 412–436. https://doi.org/10.1038/s41588-022-01024-z.

51. Lambert, J.C., Ibrahim-Verbaas, C.A., Harold, D., Naj, A.C., Sims, R., Bellenguez, C., DeStafano, A.L., Bis, J.C., Beecham, G.W., Grenier-Boley, B., et al. (2013). Meta-analysis of 74,046 individuals identifies 11 new susceptibility loci for Alzheimer's disease. Nat. Genet. *45*, 1452–1458. https://doi.org/10.1038/ng.2802.

52. Holstege, H., Hulsman, M., Charbonnier, C., Grenier-Boley, B., Quenez, O., Grozeva, D., van Rooij, J.G.J., Sims, R., Ahmad, S., Amin, N., et al. (2022). Exome sequencing identifies rare damaging variants in ATP8B4 and ABCA1 as risk factors for Alzheimer's disease. Nat. Genet. *54*, 1786–1794. https://doi.org/10.1038/s41588-022-01208-7.

53. Rademakers, R., Neumann, M., and Mackenzie, I.R. (2012). Advances in understanding the molecular basis of frontotemporal dementia. Nat. Rev. Neurol. *8*, 423–434. https://doi.org/10.1038/nrneurol.2012.117.

54. Brady, O.A., Zhou, X., and Hu, F. (2014). Regulated intramembrane proteolysis of the frontotemporal lobar degeneration risk factor, TMEM106B, by signal peptide peptidase-like 2a (SPPL2a). J. Biol. Chem. *289*, 19670–19680. https://doi.org/10.1074/jbc.M113.515700.

55. Chabriat, H., Joutel, A., Dichgans, M., Tournier-Lasserve, E., and Bousser, M.G. (2009). Cadasil. Lancet Neurol. *8*, 643–653. https://doi.org/10.1016/S1474-4422(09)70127-9.

56. Escott-Price, V., and Hardy, J. (2022). Genome-wide association studies for Alzheimer's disease: bigger is not always better. Brain Commun. *4*, fcac125. https://doi.org/10.1093/braincomms/fcac125.

57. Andrews, S.J., Fulton-Howard, B., and Goate, A. (2020). Interpretation of risk loci from genome-wide association studies of Alzheimer's disease. Lancet Neurol. *19*, 326–335. https://doi.org/10.1016/S1474-4422(19)30435-1.

58. Modeste, E.S., Ping, L., Watson, C.M., Duong, D.M., Dammer, E.B., Johnson, E.C.B., Roberts, B.R., Lah, J.J., Levey, A.I., and Seyfried, N.T. (2023). Quantitative proteomics of cerebrospinal fluid from African Americans and Caucasians reveals shared and divergent changes in Alzheimer's disease. Mol. Neurodegener. *18*, 48. https://doi.org/10.1186/s13024-023-00638-z.

59. Watson, C.M., Dammer, E.B., Ping, L., Duong, D.M., Modeste, E., Carter, E.K., Johnson, E.C.B., Levey, A.I., Lah, J.J., Roberts, B.R., and Seyfried, N.T. (2023). Quantitative Mass Spectrometry Analysis of Cerebrospinal Fluid Protein Biomarkers in Alzheimer's Disease. Sci. Data *10*, 261. https://doi.org/10.1038/s41597-023-02158-3.

60. van Zalm, P.W., Ahmed, S., Fatou, B., Schreiber, R., Barnaby, O., Boxer, A., Zetterberg, H., Steen, J.A., and Steen, H. (2023). Meta-analysis of published cerebrospinal fluid proteomics data identifies and validates metabolic enzyme panel as Alzheimer's disease biomarkers. Cell Rep. Med. *4*, 101005. https://doi.org/10.1016/j.xcrm.2023.101005.

61. Sung, Y.J., Yang, C., Norton, J., Johnson, M., Fagan, A., Bateman, R.J., Perrin, R.J., Morris, J.C., Farlow, M.R., Chhatwal, J.P., et al. (2023). Proteomics of brain, CSF, and plasma identifies molecular signatures for distinguishing sporadic and genetic Alzheimer's disease. Sci. Transl. Med. *15*, eabq5923. https://doi.org/10.1126/scitranslmed.abq5923.

62. Panyard, D.J., McKetney, J., Deming, Y.K., Morrow, A.R., Ennis, G.E., Jonaitis, E.M., Van Hulle, C.A., Yang, C., Sung, Y.J., Ali, M., et al. (2023). Large-scale proteome and metabolome analysis of CSF implicates altered glucose and carbon metabolism and succinylcarnitine in Alzheimer's disease. Alzheimers Dement. *19*, 5447–5470. https://doi.org/10.1002/alz.13130.

63. Johnson, E.C.B., Bian, S., Haque, R.U., Carter, E.K., Watson, C.M., Gordon, B.A., Ping, L., Duong, D.M., Epstein, M.P., McDade, E., et al. (2023). Cerebrospinal fluid proteomics define the natural history of autosomal dominant Alzheimer's disease. Nat. Med. *29*, 1979–1988. https://doi.org/10.1038/s41591-023-02476-4.

64. Visser, P.J., Reus, L.M., Gobom, J., Jansen, I., Dicks, E., van der Lee, S.J., Tsolaki, M., Verhey, F.R.J., Popp, J., Martinez-Lage, P., et al. (2022). Cerebrospinal fluid tau levels are associated with abnormal neuronal plasticity markers in Alzheimer's disease. Mol. Neurodegener. *17*, 27. https://doi.org/10.1186/s13024-022-00521-3.

65. Delvenne, A., Gobom, J., Tijms, B., Bos, I., Reus, L.M., Dobricic, V., Kate, M.T., Verhey, F., Ramakers, I., Scheltens, P., et al. (2022). Cerebrospinal fluid proteomic profiling of individuals with mild cognitive impairment and suspected non-Alzheimer's disease pathophysiology. Alzheimers Dement *19*, 807–820. https://doi.org/10.1002/alz.12713.

66. Del Campo, M., Peeters, C.F.W., Johnson, E.C.B., Vermunt, L., Hok, A.H.Y.S., van Nee, M., Chen-Plotkin, A., Irwin, D.J., Hu, W.T., Lah, J.J., et al. (2022). CSF proteome profiling across the Alzheimer's disease spectrum reflects the multifactorial nature of the disease and identifies specific biomarker panels. Nat. Aging *2*, 1040–1053. https://doi.org/10.1038/s43587-022-00300-1.

67. Dammer, E.B., Ping, L., Duong, D.M., Modeste, E.S., Seyfried, N.T., Lah, J.J., Levey, A.I., and Johnson, E.C.B. (2022). Multi-platform proteomic analysis of Alzheimer's disease cerebrospinal fluid and plasma reveals network biomarkers associated with proteostasis and the matrisome. Alzheimer's Res. Ther. *14*, 174. https://doi.org/10.1186/s13195-022-01113-5.

68. Higginbotham, L., Ping, L., Dammer, E.B., Duong, D.M., Zhou, M., Gearing, M., Hurst, C., Glass, J.D., Factor, S.A., Johnson, E.C.B., et al. (2020). Integrated proteomics reveals brain-based cerebrospinal fluid biomarkers in asymptomatic and symptomatic Alzheimer's disease. Sci. Adv. *6*, eaaz9360. https://doi.org/10.1126/sciadv.aaz9360.

69. Dawson, T.M., Golde, T.E., and Lagier-Tourenne, C. (2018). Animal models of neurodegenerative diseases. Nat. Neurosci. *21*, 1370–1379. https://doi.org/10.1038/s41593-018-0236-8.

70. Drummond, E., and Wisniewski, T. (2017). Alzheimer's disease: experimental models and reality. Acta Neuropathol. *133*, 155–175. https://doi.org/10.1007/s00401-016-1662-x.

71. Wykes, R., Kalmbach, A., Eliava, M., and Waters, J. (2012). Changes in the physiology of CA1 hippocampal pyramidal neurons in preplaque CRND8 mice. Neurobiol. Aging *33*, 1609–1623. https://doi.org/10.1016/j.neurobiolaging.2011.05.001.

72. Jolas, T., Zhang, X.S., Zhang, Q., Wong, G., Del Vecchio, R., Gold, L., and Priestley, T. (2002). Long-term potentiation is increased in the CA1 area of the hippocampus of APP(swe/ind) CRND8 mice. Neurobiol. Dis. *11*, 394–409.

73. Chakrabarty, P., Li, A., Ceballos-Diaz, C., Eddy, J.A., Funk, C.C., Moore, B., DiNunno, N., Rosario, A.M., Cruz, P.E., Verbeeck, C., et al. (2015). IL-10 alters immunoproteostasis in APP mice, increasing plaque burden and worsening cognitive behavior. Neuron *85*, 519–533. https://doi.org/10.1016/j.neuron.2014.11.020.

74. Palop, J.J., and Mucke, L. (2010). Amyloid-beta-induced neuronal dysfunction in Alzheimer's disease: from synapses toward neural networks. Nat. Neurosci. *13*, 812–818. https://doi.org/10.1038/nn.2583.

75. Selkoe, D.J., and Hardy, J. (2016). The amyloid hypothesis of Alzheimer's disease at 25 years. EMBO Mol. Med. *8*, 595–608. https://doi.org/10.15252/emmm.201606210.

76. Yu, L., Tasaki, S., Schneider, J.A., Arfanakis, K., Duong, D.M., Wingo, A.P., Wingo, T.S., Kearns, N., Thatcher, G.R.J., Seyfried, N.T., et al. (2020). Cortical Proteins Associated With Cognitive Resilience in Community-Dwelling Older Persons. JAMA Psychiatr. *77*, 1172–1180. https://doi.org/10.1001/jamapsychiatry.2020.1807.

77. Hurst, C.D., Dunn, A.R., Dammer, E.B., Duong, D.M., Seyfried, N.T., Kaczorowski, C.C., and Johnson, E.C.B. (2023). Genetic background influences the 5XFAD Alzheimer's disease mouse model brain proteome. bioRxiv. https://doi.org/10.1101/2023.06.12.544646.

78. Van Acker, Z.P., Perdok, A., Bretou, M., and Annaert, W. (2021). The microglial lysosomal system in Alzheimer's disease: Guardian against proteinopathy. Ageing Res. Rev. *71*, 101444. https://doi.org/10.1016/j.arr.2021.101444.

79. Pimplikar, S.W., Nixon, R.A., Robakis, N.K., Shen, J., and Tsai, L.H. (2010). Amyloid-independent mechanisms in Alzheimer's disease pathogenesis. J. Neurosci. *30*, 14946–14954. https://doi.org/10.1523/JNEUROSCI.4305-10.2010.

80. Castellano, J.M., Kim, J., Stewart, F.R., Jiang, H., DeMattos, R.B., Patterson, B.W., Fagan, A.M., Morris, J.C., Mawuenyega, K.G., Cruchaga, C., et al. (2011). Human apoE isoforms differentially regulate brain amyloid-beta peptide clearance. Sci. Transl. Med. *3*, 89ra57. https://doi.org/10.1126/scitranslmed.3002156.

81. Holtzman, D.M. (2004). In vivo effects of ApoE and clusterin on amyloid-beta metabolism and neuropathology. J. Mol. Neurosci. *23*, 247–254.

82. Fagan, A.M., Watson, M., Parsadanian, M., Bales, K.R., Paul, S.M., and Holtzman, D.M. (2002). Human and murine ApoE markedly alters A beta metabolism before and after plaque formation in a mouse model of Alzheimer's disease. Neurobiol. Dis. *9*, 305–318.

83. Soderberg, L., Zhukareva, V., Bogdanovic, N., Hashimoto, T., Winblad, B., Iwatsubo, T., Lee, V.M., Trojanowski, J.Q., and Naslund, J. (2003). Molecular identification of AMY, an Alzheimer disease amyloid-associated protein. J. Neuropathol. Exp. Neurol. *62*, 1108–1117. https://doi.org/10.1093/jnen/62.11.1108.

84. Hashimoto, T., Wakabayashi, T., Watanabe, A., Kowa, H., Hosoda, R., Nakamura, A., Kanazawa, I., Arai, T., Takio, K., Mann, D.M., and Iwatsubo, T. (2002). CLAC: a novel Alzheimer amyloid plaque component derived from a transmembrane precursor, CLAC-P/collagen type XXV. EMBO J. *21*, 1524–1534. https://doi.org/10.1093/emboj/21.7.1524.

85. Langfelder, P., and Horvath, S. (2008). WGCNA: an R package for weighted correlation network analysis. BMC Bioinf. *9*, 559. https://doi.org/10.1186/1471-2105-9-559.

86. Zellner, A., Muller, S.A., Lindner, B., Beaufort, N., Rozemuller, A.J.M., Arzberger, T., Gassen, N.C., Lichtenthaler, S.F., Kuster, B., Haffner, C., and Dichgans, M. (2022). Proteomic profiling in cerebral amyloid angiopathy reveals an overlap with CADASIL highlighting accumulation of HTRA1 and its substrates. Acta Neuropathol. Commun. *10*, 6. https://doi.org/10.1186/s40478-021-01303-6.

87. Hondius, D.C., Eigenhuis, K.N., Morrema, T.H.J., van der Schors, R.C., van Nierop, P., Bugiani, M., Li, K.W., Hoozemans, J.J.M., Smit, A.B., and Rozemuller, A.J.M. (2018). Proteomics analysis identifies new markers associated with capillary cerebral amyloid angiopathy in Alzheimer's disease. Acta Neuropathol. Commun. *6*, 46. https://doi.org/10.1186/s40478-018-0540-2.

88. Wojtas, A.M., Dammer, E.B., Guo, Q., Ping, L., Shantaraman, A., Duong, D.M., Yin, L., Fox, E.J., Seifar, F., Lee, E.B., et al. (2024). Proteomic Changes in the Human Cerebrovasculature in Alzheimer's Disease and Related Tauopathies Linked to Peripheral Biomarkers in Plasma and Cerebrospinal Fluid. medRxiv. https://doi.org/10.1101/2024.01.10.24301099.

89. Zellner, A., Scharrer, E., Arzberger, T., Oka, C., Domenga-Denier, V., Joutel, A., Lichtenthaler, S.F., Muller, S.A., Dichgans, M., and Haffner, C. (2018). CADASIL brain vessels show a HTRA1 loss-of-function profile. Acta Neuropathol. *136*, 111–125. https://doi.org/10.1007/s00401-018-1853-8.

90. Cerezo-Wallis, D., Contreras-Alcalde, M., Troule, K., Catena, X., Mucientes, C., Calvo, T.G., Canon, E., Tejedo, C., Pennacchi, P.C., Hogan, S., et al. (2020). Midkine rewires the melanoma microenvironment toward a tolerogenic and immune-resistant state. Nat. Med. *26*, 1865–1877. https://doi.org/10.1038/s41591-020-1073-3.

91. Tang, Y., Kwiatkowski, D.J., and Henske, E.P. (2022). Midkine expression by stem-like tumor cells drives persistence to mTOR inhibition and an immune-suppressive microenvironment. Nat. Commun. *13*, 5018. https://doi.org/10.1038/s41467-022-32673-7.

92. Shen, D., Podolnikova, N.P., Yakubenko, V.P., Ardell, C.L., Balabiyev, A., Ugarova, T.P., and Wang, X. (2017). Pleiotrophin, a multifunctional cytokine and growth factor, induces leukocyte responses through the integrin Mac-1. J. Biol. Chem. *292*, 18848–18861. https://doi.org/10.1074/jbc.M116.773713.

93. Muramatsu, H., Yokoi, K., Chen, L., Ichihara-Tanaka, K., Kimura, T., and Muramatsu, T. (2011). Midkine as a factor to counteract the deposition of amyloid beta-peptide plaques: in vitro analysis and examination in knockout mice. Int. Arch. Med. *4*, 1. https://doi.org/10.1186/1755-7682-4-1.

94. Snow, A.D., Cummings, J.A., and Lake, T. (2021). The Unifying Hypothesis of Alzheimer's Disease: Heparan Sulfate Proteoglycans/Glycosaminoglycans Are Key as First Hypothesized Over 30 Years Ago. Front. Aging Neurosci. *13*, 710683. https://doi.org/10.3389/fnagi.2021.710683.

95. Vaquer-Alicea, J., and Diamond, M.I. (2019). Propagation of Protein Aggregation in Neurodegenerative Diseases. Annu. Rev. Biochem. *88*, 785–810. https://doi.org/10.1146/annurev-biochem-061516-045049.

96. Kourelis, T.V., Dasari, S.S., Dispenzieri, A., Maleszewski, J.J., Redfield, M.M., Fayyaz, A.U., Grogan, M., Ramirez-Alvarado, M., Abou Ezzeddine, O.F., and McPhail, E.D. (2020). A Proteomic Atlas of Cardiac Amyloid Plaques. JACC. CardioOncol. *2*, 632–643. https://doi.org/10.1016/j.jaccao.2020.08.013.

97. Rahman, M.M., and Lendel, C. (2021). Extracellular protein components of amyloid plaques and their roles in Alzheimer's disease pathology. Mol. Neurodegener. *16*, 59. https://doi.org/10.1186/s13024-021-00465-0.

98. Wagner, J., Degenhardt, K., Veit, M., Louros, N., Konstantoulea, K., Skodras, A., Wild, K., Liu, P., Obermuller, U., Bansal, V., et al. (2022). Medin co-aggregates with vascular amyloid-beta in Alzheimer's disease. Nature *612*, 123–131. https://doi.org/10.1038/s41586-022-05440-3.

99. Venegas, C., Kumar, S., Franklin, B.S., Dierkes, T., Brinkschulte, R., Tejera, D., Vieira-Saecker, A., Schwartz, S., Santarelli, F., Kummer, M.P., et al. (2017). Microglia-derived ASC specks cross-seed amyloid-beta in Alzheimer's disease. Nature *552*, 355–361. https://doi.org/10.1038/nature25158.

100. Yakupova, E.I., Bobyleva, L.G., Shumeyko, S.A., Vikhlyantsev, I.M., and Bobylev, A.G. (2021). Amyloids: The History of Toxicity and Functionality. Biology *10*, 394. https://doi.org/10.3390/biology10050394.

101. Walsh, D.M., and Selkoe, D.J. (2004). Deciphering the molecular basis of memory failure in Alzheimer's disease. Neuron *44*, 181–193.

102. Dobson, C.M., Knowles, T.P.J., and Vendruscolo, M. (2020). The Amyloid Phenomenon and Its Significance in Biology and Medicine. Cold Spring Harb. Perspect. Biol. *12*, a033878. https://doi.org/10.1101/cshperspect.a033878.

103. Papadimitriou, E., Mourkogianni, E., Ntenekou, D., Christopoulou, M., Koutsioumpa, M., and Lamprou, M. (2022). On the role of pleiotrophin and its receptors in development and angiogenesis. Int. J. Dev. Biol. *66*, 115–124. https://doi.org/10.1387/ijdb.210122ep.

104. Weckbach, L.T., Grabmaier, U., Uhl, A., Gess, S., Boehm, F., Zehrer, A., Pick, R., Salvermoser, M., Czermak, T., Pircher, J., et al. (2019). Midkine drives cardiac inflammation by promoting neutrophil trafficking and NETosis in myocarditis. J. Exp. Med. *216*, 350–368. https://doi.org/10.1084/jem.20181102.

105. Woulfe, K.C., and Sucharov, C.C. (2017). Midkine's Role in Cardiac Pathology. J. Cardiovasc. Dev. Dis. *4*, 13. https://doi.org/10.3390/jcdd4030013.

106. Rubel, M.S., Fedotov, S.A., Grizel, A.V., Sopova, J.V., Malikova, O.A., Chernoff, Y.O., and Rubel, A.A. (2020). Functional Mammalian Amyloids and Amyloid-Like Proteins. Life *10*, 156. https://doi.org/10.3390/life10090156.

107. Venegas, C., and Heneka, M.T. (2017). Danger-associated molecular patterns in Alzheimer's disease. J. Leukoc. Biol. *101*, 87–98. https://doi.org/10.1189/jlb.3MR0416-204R.

108. Golde, T.E. (2019). Harnessing Immunoproteostasis to Treat Neurodegenerative Disorders. Neuron *101*, 1003–1015. https://doi.org/10.1016/j.neuron.2019.02.027.

109. Pinals, R.L., and Tsai, L.H. (2022). Building in vitro models of the brain to understand the role of APOE in Alzheimer's disease. Life Sci. Alliance *5*, e202201542. https://doi.org/10.26508/lsa.202201542.

110. Martens, Y.A., Zhao, N., Liu, C.C., Kanekiyo, T., Yang, A.J., Goate, A.M., Holtzman, D.M., and Bu, G. (2022). ApoE Cascade Hypothesis in the pathogenesis of Alzheimer's disease and related dementias. Neuron *110*, 1304–1317. https://doi.org/10.1016/j.neuron.2022.03.004.

111. Xiong, M., Jiang, H., Serrano, J.R., Gonzales, E.R., Wang, C., Gratuze, M., Hoyle, R., Bien-Ly, N., Silverman, A.P., Sullivan, P.M., et al. (2021). APOE immunotherapy reduces cerebral amyloid angiopathy and amyloid plaques while improving cerebrovascular function. Sci. Transl. Med. *13*, eabd7522. https://doi.org/10.1126/scitranslmed.abd7522.

112. Wang, H., Dey, K.K., Chen, P.C., Li, Y., Niu, M., Cho, J.H., Wang, X., Bai, B., Jiao, Y., Chepyala, S.R., et al. (2020). Integrated analysis of ultra-deep proteomes in cortex, cerebrospinal fluid and serum reveals a mitochondrial signature in Alzheimer's disease. Mol. Neurodegener. *15*, 43. https://doi.org/10.1186/s13024-020-00384-6.

113. Allen, M., Wang, X., Burgess, J.D., Watzlawik, J., Serie, D.J., Younkin, C.S., Nguyen, T., Malphrus, K.G., Lincoln, S., Carrasquillo, M.M., et al. (2018). Conserved brain myelination networks are altered in Alzheimer's and other neurodegenerative diseases. Alzheimers Dement. *14*, 352–366. https://doi.org/10.1016/j.jalz.2017.09.012.

114. Nikolayeva, O., and Robinson, M.D. (2014). edgeR for differential RNA-seq and ChIP-seq analysis: an application to stem cell biology. Methods Mol. Biol. *1150*, 45–79. https://doi.org/10.1007/978-1-4939-0512-6_3.

115. Moore, B.D., Ran, Y., Goodwin, M.S., Komatineni, K., McFarland, K.N., Dillon, K., Charles, C., Ryu, D., Liu, X., Prokop, S., et al. (2023). A C1qTNF3 collagen domain fusion chaperones diverse secreted proteins and anti-Aβ scFvs: applications for gene therapies. Mol. Ther. Methods Clin. Dev. *31*, 101146. https://doi.org/10.1016/j.omtm.2023.101146.

116. Chakrabarty, P., Jansen-West, K., Beccard, A., Ceballos-Diaz, C., Levites, Y., Verbeeck, C., Zubair, A.C., Dickson, D., Golde, T.E., and Das, P. (2010). Massive gliosis induced by interleukin-6 suppresses Abeta deposition in vivo: evidence against inflammation as a driving force for amyloid deposition. FASEB J *24*, 548–559. https://doi.org/10.1096/fj.09-141754.

117. Xu, G., Ran, Y., Fromholt, S.E., Fu, C., Yachnis, A.T., Golde, T.E., and Borchelt, D.R. (2015). Murine Aβ over-production produces diffuse and compact Alzheimer-type amyloid deposits. Acta Neuropathol. Commun. *3*, 72. https://doi.org/10.1186/s40478-015-0252-9.

118. Levites, Y., Das, P., Price, R.W., Rochette, M.J., Kostura, L.A., McGowan, E.M., Murphy, M.P., and Golde, T.E. (2006). Anti-Abeta42- and anti-Abeta40-specific mAbs attenuate amyloid deposition in an Alzheimer disease mouse model. J. Clin. Invest. *116*, 193–201. https://doi.org/10.1172/JCI25410.

119. Montine, T.J., Phelps, C.H., Beach, T.G., Bigio, E.H., Cairns, N.J., Dickson, D.W., Duyckaerts, C., Frosch, M.P., Masliah, E., Mirra, S.S., et al. (2012). National Institute on Aging-Alzheimer's Association guidelines for the neuropathologic assessment of Alzheimer's disease: a practical approach. Acta Neuropathol. *123*, 1–11. https://doi.org/10.1007/s00401-011-0910-3.

120. Moore, B.D., Levites, Y., Xu, G., Hampton, H., Adamo, M.F., Croft, C.L., Futch, H.S., Moran, C., Fromholt, S., Janus, C., et al. (2022). Soluble brain homogenates from diverse human and mouse sources preferentially seed diffuse Aβ plaque pathology when injected into newborn mouse hosts. Free Neuropathol. *3*, 3-9. https://doi.org/10.17879/freeneuropathology-2022-3766.

121. Naiki, H., Higuchi, K., Nakakuki, K., and Takeda, T. (1991). Kinetic analysis of amyloid fibril polymerization in vitro. Lab. Invest. *65*, 104–110.

122. Dobin, A., Davis, C.A., Schlesinger, F., Drenkow, J., Zaleski, C., Jha, S., Batut, P., Chaisson, M., and Gingeras, T.R. (2013). STAR: ultrafast universal RNA-seq aligner. Bioinformatics *29*, 15–21. https://doi.org/10.1093/bioinformatics/bts635.

123. Lawrence, M., Huber, W., Pages, H., Aboyoun, P., Carlson, M., Gentleman, R., Morgan, M.T., and Carey, V.J. (2013). Software for computing and annotating genomic ranges. PLoS Comput. Biol. *9*, e1003118. https://doi.org/10.1371/journal.pcbi.1003118.

124. Love, M.I., Huber, W., and Anders, S. (2014). Moderated estimation of fold change and dispersion for RNA-seq data with DESeq2. Genome Biol. *15*, 550. https://doi.org/10.1186/s13059-014-0550-8.

125. Young, M.D., Wakefield, M.J., Smyth, G.K., and Oshlack, A. (2010). Gene ontology analysis for RNA-seq: accounting for selection bias. Genome Biol. *11*, R14. https://doi.org/10.1186/gb-2010-11-2-r14.

STAR★METHODS

KEY RESOURCES TABLE

REAGENT or RESOURCE	SOURCE	IDENTIFIER
Antibodies		
mouse monoclonal Pan- Ab	T. Golde, Emory University	Ab5
Rabbit polyclonal amyloid fibrils	Novus	NBP1-97929; RRID: AB_3134150
mouse monoclonal Ab42	T. Golde, Emory University	2.1.3
mouse monoclonal Ab40	T. Golde, Emory University	13.1.1
rabbit polyclonal Col25a1	this paper	N/A
rabbit polyclonal Slit2	Invitrogen	PA531133; RRID:AB_2548607
rabbit polyclonal Mdk	this paper	N/A
sheep polyclonal Mdk	Novus Biologicals	AF7769; RRID:AB_2917965
rabbit monoclonal Mdk	Abcam	ab52637; RRID:AB_880698
rabbit polyclonal Vtn	this paper	N/A
rabbit polyclonal Ptn	this paper	N/A
rabbit monoclonal Ptn	Abcam	ab79411; RRID:AB_1603350
rabbit polyclonal Dmp1	this paper	N/A
rabbit polyclonal Olfml3	this paper	N/A
rabbit polyclonal Htra1	this paper	N/A
rabbit polyclonal Smoc1	this paper	N/A
rabbit polyclonal Sulf1	Invitrogen	PA5-115984; RRID:AB_2900618
rabbit polyclonal Sfrp1	this paper	N/A
rabbit polyclonal Ndp	this paper	N/A
rabbit polyclonal Ndp	Thermofisher	PA5-102534; RRID:AB_2851936
rabbit polyclonal Hgf	this paper	N/A
rabbit polyclonal Sdc4	this paper	N/A
rabbit polyclonal Ntn1	this paper	N/A
rabbit polyclonal HHIPL1	this paper	N/A
rabbit polyclonal HHIPL1	Invitrogen	PA5-62678; RRID:AB_2642422
rabbit polyclonal Spock3	this paper	N/A
rabbit polyclonal S100a6	this paper	N/A
rabbit polyclonal S100a6	Thermofisher	MA5-32511; RRID:AB_2809788
rabbit polyclonal Ctss	Thermofisher	PA5-115062; RRID:AB_2899698
rabbit polyclonal Bmp6	this paper	N/A
rabbit polyclonal Frzb	this paper	N/A
rabbit polyclonal Sema3e	this paper	N/A
rabbit polyclonal Spock1	this paper	N/A
rabbit polyclonal Apod	this paper	N/A
rabbit polyclonal Egfl8	this paper	N/A
rabbit polyclonal C1qTnf4	this paper	N/A
rabbit polyclonal Flt1	this paper	N/A
rabbit polyclonal Flt1	Thermofisher	PA5-99362; RRID:AB_2818295
rabbit polyclonal Smoc2	this paper	N/A
rabbit polyclonal Nog	this paper	N/A
rabbit polyclonal Slit3	this paper	N/A
rat monoclonal Flag	Sigma	SAB4200071; RRID:AB_10603396
mouse monoclonal-b-actin	Millipore-Sigma	ZRB1312; RRID:AB_3083534

(*Continued on next page*)

Continued

REAGENT or RESOURCE	SOURCE	IDENTIFIER
Alexa Fluor-680 or Alexa Fluor-800 secondary Abs	Invitrogen	N/A
Bacterial and virus strains		
pAAV	T. Golde, Emory University	N/A
NEB Stable	NEB	C3040H
Biological samples		
AD frontal cortex tissue	1Florida ADRC brain bank	https://mbi.ufl.edu/
Human Cardiac Amyloidosis	Dr. Frank Heppner	N/A
Chemicals, peptides, and recombinant proteins		
Protease inhibitor cocktail	Millipore	539131
DAB Substrate Kit	Vector labs	SK-4100
ImmPRESS HRP secondary antibodies	Vector labs	MP-7802-15, MP-7801-15
Hematoxylin	Sigma Aldrich	Mayer's version
Cytoseal	Thermo Fisher	N/A
Bolt 4-12% Bis-Tris gels	Thermo Fisher	NW0412BOX
Thioflavin T	Millipore Sigma	T3516-5G
Ab1-42	rPeptide	A-1170-1
iBlot 2 dry blotting system	Thermo Fisher	IB21001
Laemmli sample buffer	BioRad	161-0737
Critical commercial assays		
TMT 11-plex kit	ThermoFisher	90406 – Lot#TG273545 and TG273555
TMTPro	ThermoFisher	A44520 – Lot# VH311511
Trizol	Fisher	15596026
Qiagen RNeasy miniprep kit	Qiagen	74104
Aglient RNA 6000 Nano Kit	Agilent	5067-1511
TruSeq RNA Sample Prep Kit v2	Illumina	RS-122-2001
SuperScript II RT	Invitrogen	18064-014
Agencourt AMPure XP	Beckman Coulter Genomics	A63881
Kapa Library Quantification Kit, Illumina library, BioRad qPCR	Kapa Biosystems	KK4844
NextSeq 500/550 High Output v2.5 kit, 150 cycles	Illumina	20024907
Deposited data		
RNA-sequencing data (fastq files) for CRND8, 18mon brains	Synapse.org	syn27057871
Experimental models: Cell lines		
HEK293T	ATCC	CRL-3216
Experimental models: Organisms/strains		
Mouse: B6C3F1/J	The Jackson labs	Jax: Strain #:**100010**
Mouse:CRND8	Chishti MA, 2001	N/A
Recombinant DNA		
pCDNA3.1	T. Golde, Emory University	N/A
rAAV2-CBA expression vector pCTR4	T. Golde, Emory University	N/A
pDP8.ape	PlasmidFactory	PF0478
rAAV-Mdk	Genescript	N/A
rAAV-PTN	Genescript	N/A
Software and algorithms		
ImageJ1.53k		https://imagej.nih.gov/ij/

(*Continued on next page*)

Continued

REAGENT or RESOURCE	SOURCE	IDENTIFIER
ImageScope	Leica Biosystems	https://www.leicabiosystems.com/us/digital-pathology/manage/aperio-imagescope/
Synthetic Eigenprotein Calculator	E. Dammer	Upon request to author
One-tailed Fisher's Exact Implementation for enrichment of cell type markers in network modules	E. Dammer	https://www.github.com/edammer/CellTypeFET/
Circular heatmap graphical representation of eigenprotein groupwise significance, cell type marker enrichment, trait correlations (bicor) by module using R package circlize v0.4.15	E. Dammer	Upon request to author
Other		
BioRender	N/A	https://biorender.com/
GraphPad Prism 9		N/A
Softmax Pro	Molecular Devices	N/A
R v4.2.3	The Comprehensive R Archive Network	https://cran.r-project.org/
ggplot2	Wickham et al.	https://ggplot2.tidyverse.org/

RESOURCE AVAILABILITY

Lead contact

Further information and requests for resources and reagents should be directed to and will be fulfilled by the lead contact, Todd E. Golde (tgolde@emory.edu).

Materials availability

Plasmids generated in this study will be available upon request.

Data and code availability

- **AD Knowledge Portal: AMP-AD datasets:** The results published here are in whole or in part based on data obtained from the AMP-AD Knowledge Portal (https://doi.org/10.7303/syn2580853). Mayo Clinic: The Mayo RNAseq study data was led by Dr. Nilüfer Ertekin-Taner, Mayo Clinic, Jacksonville, FL as part of the multi-PI U01 AG046139 (MPIs Golde, Ertekin-Taner, Younkin, Price). Samples were provided from the following sources: The Mayo Clinic Brain Bank and Banner Sun Health Research Institute. Data collection was supported through funding by NIA grants P50 AG016574, R01 AG032990, U01 AG046139, R01 AG018023, U01 AG006576, U01 AG006786, R01 AG025711, R01 AG017216, R01 AG003949, NINDS grant R01 NS080820, CurePSP Foundation, and support from Mayo Foundation. Study data includes samples collected through the Sun Health Research Institute Brain and Body Donation Program of Sun City, Arizona. The Brain and Body Donation Program is supported by the National Institute of Neurological Disorders and Stroke (U24 NS072026 National Brain and Tissue Resource for Parkinson's Disease and Related Disorders), the National Institute on Aging (P30 AG19610 Arizona Alzheimer's Disease Core Center), the Arizona Department of Health Services (contract 211002, Arizona Alzheimer's Research Center), the Arizona Biomedical Research Commission (contracts 4001, 0011, 05–901 and 1001 to the Arizona Parkinson's Disease Consortium) and the Michael J. Fox Foundation for Parkinson's Research. For the human protein data All raw data, case traits, and analyses (differential and co-expression) related to this manuscript are available at https://www.synapse.org/consensus. The results published here are in whole or in part based on data obtained from the AMP-AD Knowledge Portal (https://adknowledgeportal.synapse.org). The AMP-AD Knowledge Portal is a platform for accessing data, analyses, and tools generated by the Accelerating Medicines Partnership (AMP-AD) Target Discovery Program and other National Institute on Aging (NIA)-supported programs to enable open-science practices and accelerate translational learning. The data, analyses, and tools are shared early in the research cycle without a publication embargo on secondary use. Data is available for general research use according to the following requirements for data access and data attribution (https://adknowledgeportal.synapse.org/#/DataAccess/Instructions). ROSMAP resources can be requested at www.radc.rush.edu.
- Raw mass spectrometry data and pre- and post-processed plasma protein abundance data and case traits are available at https://synapse.org/CRND8. The results published here are in whole or in part based on data obtained from the AMP-AD Knowledge Portal (https://adknowledgeportal.synapse.org). The AMP-AD Knowledge Portal is a platform for accessing data, analyses, and tools generated by the AMP-AD Target Discovery Program supported by the National Institute on Aging

to enable open-science practices and accelerate translational learning. Data are available for general research use (https://adknowledgeportal.synapse.org/#/DataAccess/Instructions).

Mayo RNAseq dataset comprises transcriptome measures from temporal cortex (TCX, superior temporal gyrus) and cerebellum (CER) the former of which was utilized in this study. For non-Tg mice and CRND8 mice a sagitally dissected whole hemibrain was used. RNA isolation, data collection, sequencing alignment, counting and QC has been described in detail elsewhere.[11,34,113] EdgeR was used to reprocess both the mouse and human RNA sequencing data.[114] Mouse and human orthologues were identified in a two-step process. Most orthologous genes were first identified using http://alliancegenome.org/downloads, Database Version: 5.4.0 on Apr 20, 2023, with "Orthology Filter: Stringent". Then a manual curation of additional orthologues was conducted using the gOrth serac function on the g:profiler website (https://biit.cs.ut.ee/gprofiler/orth). Human brain proteomic data was utilized from previous publications. The human proteome data is available at Synapse (https://www.synapse.org/#!Synapse:syn20933797/wiki/596247).

- This paper does not report original code. All custom code used for the analyses was written with existing software as detailed in the STAR Methods section and is available upon request.
- Any additional information required to reanalyze the data reported in this paper is available from the lead contact upon request.

EXPERIMENTAL MODELS AND SUBJECT DETAILS

Human subjects

Postmortem brain tissues were selected from the University of Florida Human Brain and Tissue Bank (UF HBTB).[40] All protocols were approved by the University of Florida Institutional Review Board. For transthyretin amyloidosis tissues, autopsies were undertaken, and respective tissue was collected in accordance with the §1 and §4 SRegG BE of the autopsy act of Berlin, Germany.

Cell lines

HEK293T cells were purchased from ATCC (CRL-3216). They were maintained in 2D adherent culture within DMEM/F-12 (Gibco) supplemented with 10% FBS, 1% Penicillin-Streptomycin (Gibco), 1% Sodium Pyruvate (Gibco), 1% Sodium Bicarbonate (Gibco), 1% Non-Essential Amino Acids (Gibco) and 1% HEPES (Gibco). Cell passaging was performed at 1/10 twice a week. Used cells were controlled for mycoplasma-free status.

Animal models

All animal procedures were approved by the Institutional Animal Care and Use Committee in accordance with NIH guidelines. CRND8 mice were bred in-house and housed three to five to a cage and maintained on *ad libitum* food and water with a 12h light/dark cycle√.

METHOD DETAILS

Cloning

All cDNAs used were synthesized by Genscript (Piscataway, NJ) and subcloned into pCDNA3.1 vector, the rAAV2-CBA expression vector pCTR4,[115] or both. All cDNAs incorporated an FLAG epitope tag (DYKDDDDK) on the -COOH terminal. To overexpress the genes, 2.7 μg plasmid was transiently transfected into HEK 293T cells in a 6-well dish using polyethylenimine (PEI). Media was replaced with FBS free Opti-MEM after 18 h incubation. Cells and conditioned media were collected after another 24-h incubation. Bis-Tris precast gels (Bio-Rad, Hercules, CA) were used for all SDS-PAGE. 50 μg cell lysate by total protein and 30 μL media of each sample were loaded. Western blot was developed using monoclonal anti-FLAG M2 antibody and anti-β-actin (Sigma-Aldrich, Inc, St. Louis, MO).

Neonatal injections

Intracerebroventricular injections of recombinant adeno-associated virus (rAAVs) were carried out on day P0 as described previously.[116] Two microliters of rAAV2/1 encoding Mdk and PTN was administrated bilaterally into the cerebral ventricle. Mice injected with rAAV encoding MDK and PTN were aged 3 or 6 months and euthanized, brains were harvested and one hemibrain was fixed overnight in 4% paraformaldehyde at 4°C followed by processing and paraffin embedding for immunohistochemical staining. The other hemibrain was snap-frozen in isopentane on dry ice and then stored at −80°C until it was thawed and homogenized for ELISA measurements of Aβ peptide levels.

Mouse brain histology and immunohistochemistry

Paraffin sections (5 μm) were used for all histology and immunohistochemistry studies. For various antibodies screens two hemibrains from the same mouse were fixed in EtOH or in 4% PFA (alternatively, in 10% Formalin) and embedded into the same block. Antibodies used are listed in Table S10. The slides were scanned by Aperio XT System (Leica Biosystems, Buffalo Grove, IL). Thio-S tissue staining methods were performed as previously described.[117] For studies in mice injected with pAAV-Mdk or pAAV-PTN, embedded sections were immunohistochemically stained with a biotinylated pan-Aβ antibody Ab5[118] (1:500) or anti-FLAG antibody

(Sigma-Aldrich Inc, St. Louis, IL) and developed using Vectastain Elite ABC Kit (Vector Laboratories, Burlingame, CA) followed with 3,3′-diaminobenzidine (DAB) substrate (Vector Laboratories, Burlingame, CA) and counterstained with hematoxylin. The slides were scanned by Aperio XT System and analyzed using the ImageScope program. In brief, at least three sections per sample, at least 30 μm apart, were imaged and plaque burden was quantified. For three-month-old mice, the plaque number was calculated by two independent observers.

Human tissue histology and immunohistochemistry

The NIA-AA guideline for pathological diagnosis constitutes the Thal phase of Aβ plaques (A), Braak and Braak NFT stage (B), and CERAD neuritic plaque score (C) – "ABC" score – for determining ADNC[119] and cases were grouped into "no AD" (2 cases), "low AD" (18 cases), "intermediate AD" (22 cases), and "high AD" (21 cases). All cases included in this study were negative for significant Lewy body pathology or TDP-43 pathology. Control cases were classified as "no AD" following NIA-AA guidelines[119] and were also negative for significant Lewy body pathology or TDP-43 pathology. Detailed description of cases used is in.[40] 5 μm thick sections of formalin-fixed or ethanol fixed, paraffin-embedded postmortem brain tissue was deparaffinized in xylene twice for 5 min and followed by rehydration in descending ethanol series (100%, 100%, 90%, 70%) for 1 min each. For Formic acid antigen retrieval, sections were immersed in a 70% Formic acid solution for 20 min (where indicated in Table S11). Sections were incubated in 0.1M Tris and 0.005% Tween (or Citrate buffer, where indicated in Table S11) at high pressure in a pressure cooker for 15 min, followed by incubation in a PBS/H_2O_2 solution with 10% Triton X- for 20 min to quench endogenous peroxidase. The sections were washed with tap water and then equilibrated to 0.1M Tris for 5 min before blocking in normal horse serum for 20 min, followed by blocking in 2% FBS/0.1 M Tris, (pH 7.6) for 5 min. After that, primary antibody, diluted in 2% FBS/0.1 M Tris, (pH 7.6) was applied to the section and incubated overnight at 4°C. Dilutions for each antiserum is listed in Table S11. The next day, sections were quickly rinsed in 0.1M Tris and blocked in 2% FBS/0.1 M Tris, (pH 7.6) for 5 min before incubating with the secondary antibody (HRP-conjugated ImmPRESS Polymer Reagent, Vector Labs) for 30 min at room temperature. Following a quick wash in 0.1M Tris, the signal was developed using 3,3′-diaminobenzidin (DAB, Vector Lab SK-410) for 1–2 min and then sections were counterstained with hematoxylin (Mayer's version, Sigma Aldrich) for 1 min. Next, sections were washed in tap water, and then dehydrated in an ascending series of ethanol (70%, 90%, 100%, 100%) for 1 min each, followed by xylene (2 × 5 min). Sections were cover slipped using Cytoseal 60 (Thermo Fisher) mounting media and dried overnight.

Quantification of area covered (human tissue)

Images of stained slides were captured using Leica Aperio AT2 and percent positive area of immunostained slides was quantified using QuPath Software (version 0.4.3) with the Positive Pixel Count (deprecated) that detects DAB staining. The customized threshold for all immunohistochemical stains included a Downsample factor of 4.0, Gaussian sigma of 2–4 μm, Hematoxylin threshold of 1 OD unit. The only variable factor across the different antibody stains was the DAB threshold. All statistical analysis is conducted in GraphPad Prism (v9.5.1). One-way ANOVA with Tukey's multiple comparisons test was carried out to compare the percent area covered by each AAP in Low AD, Intermediate AD, and High AD cases defined by "ABC" severity score.

Aβ ELISAs

After tissue harvesting, the left hemisphere was flash-frozen in isopentane. The frozen cortex was sequentially extracted with protease inhibitor cocktail (Roche, Basel, Switzerland) containing RIPA buffer, 2% SDS, and 70% formic acid (FA) as described previously at a concentration of 150 mg/mL. Aβ levels from the 2% SDS– and 70% FA–extracted samples were quantified using end-specific sandwich ELISA as previously described.[120] Aβ40 was captured with mAb 13.1.1 and detected by HRP-conjugated mAb5. Aβ42 was captured with mAb 2.1.3 and detected by HRP-conjugated mAb5. ELISA results were analyzed using SoftMax Pro software (Molecular Devices, San Jose, CA).

Amyloid-β aggregation assay

The effect of midkine (MDK) and pleiotrophin (PTN) proteins on amyloid beta 1–42 ($Aβ_{1-42}$) aggregation was measured by *in vitro* thioflavin T (ThT) fluorescence assay, as previously described.[121] Recombinant human $Aβ_{1-42}$ (20 ng/μL equivalent to 5 μM) from rPeptide (A-1170-1) was incubated in Tris-buffered Saline (TBS; 150 mM NaCl, 50 mM Tris-HCl, pH 7.6), and 20 μM ThT in the presence or absence of purified recombinant MDK (1.25 ng/μL equivalent to 47 nM) from Sino Biological (10247-HNAB) or PTN (5 ng/μL equivalent to 327 nM) from R&D Systems (R&D252-PL-050). The final volume within each well was 100 μL. The assay was conducted in quadruplicates using chilled (4°C) 96 well black clear bottom plates (Corning, #3904). Fluorescence was captured at 420 Ex, 480 Em for 20 h at 15 min intervals at 37°C using Synergy H1 (Biotek) microplate reader. ThT alone (20 μM) was measured and subtracted as background fluorescence. A titration curve was also performed with fixed concentration of $Aβ_{1-42}$ (5 μM) and an increasing concentration of MDK (12 nM, 23 nM, 47 nM and 93 nM) or PTN (82 nM 163 nM and 327 nM). Fluorescence intensities were graphed using GraphPad Prism.

Pulldowns and western blot analysis

$Aβ_{1-42}$ fibrils prepared as described above (20 h incubation) were precipitated by centrifugation at 10,000 x g. The pellet was resuspended in 8M urea buffer (8 M urea, 100 mm $NaHPO_4$, pH 8.5) and boiled in Laemmli sample buffer (BioRad, 161–0737) at 98°C for

5 min. Proteins were resolved on Bolt 4–12% Bis-Tris gels (Thermo Fisher Scientific, NW04120BOX) followed by transfer to nitrocellulose membrane using iBlot 2 dry blotting system (ThermoFisher Scientific, IB21001). Membranes were incubated with StartingBlock buffer (ThermoFisher, 37543) for 30 min followed by overnight incubation at 4° in primary antibodies including Aβ (Novus, NBP11-97929), MDK (Abcam, #52637), and PTN (Abcam, #ab79411) antibodies. Membranes were washed with TBS containing 0.1% (v/v) Tween 20 (TBS-T) and incubated with fluorophore-conjugated secondary antibodies (Alexa Fluor 680 or Alexa Fluor 800; Invitrogen) for 1 h at room temperature. Membranes were subsequently washed three times with TBS-T and images were captured using an Odyssey Infrared Imaging System (LI-COR Biosciences).

Proteomic sample processing

Each tissue piece was individually homogenized in 300 μL of urea lysis buffer (8M urea, 100 mM $NaHPO_4$, pH 8.5), including 3 μL (100x stock) HALT protease and phosphatase inhibitor cocktail (Pierce). All homogenization was performed using a Bullet Blender (Next Advance) according to manufacturer protocols. Briefly, each tissue piece was added to Urea lysis buffer in a 1.5 mL Rino tube (Next Advance) harboring 500 mg stainless steel beads (0.9–2 mm in diameter) and blended twice for 5-min intervals in the cold room (4°C). Protein supernatants were transferred to 1.5 mL Eppendorf tubes and sonicated (Sonic Dismembrator, Fisher Scientific) 3 times for 5 s with 15 s intervals of rest at 30% amplitude to disrupt nucleic acids and subsequently vortexed. Protein concentration was determined by the bicinchoninic acid (BCA) method, and samples were frozen in aliquots at −80°C. Protein homogenates (100 μg) were diluted with 50 mM NH_4HCO_3 to a final concentration of less than 2M urea and then treated with 1 mM dithiothreitol (DTT) at 25°C for 30 min, followed by 5 mM iodoacetimide (IAA) at 25°C for 30 min in the dark. Protein was digested with 1:100 (w/w) lysyl endopeptidase (Wako) at 25°C for 2 h and further digested overnight with 1:50 (w/w) trypsin (Promega) at 25°C. Resulting peptides were desalted with a Sep-Pak C18 column (Waters) and dried under vacuum.

Tandem mass tag (TMT) labeling

Batches 1 and 2 were labeled using the TMT 11-plex kit (ThermoFisher 90406 – Lot# TG273545 and TG273555) while batch 3 was labeled with TMTPro (ThermoFisher A44520 – Lot# VH311511) according to manufacturer's protocol. For batches 1 and 2, each sample (containing 100 μg of peptides) was re-suspended in 100 mM TEAB buffer (100 μL). The TMT labeling reagents were equilibrated to room temperature, and anhydrous ACN (256 μL) was added to each reagent channel. Each channel was gently vortexed for 5 min, and then 41 μL from each TMT channel was transferred to the peptide solutions and allowed to incubate for 1 h at room temperature. The reaction was quenched with 5% (v/v) hydroxylamine (8 μL) (Pierce). For batch 3, each sample (containing 100 μg of peptides) was re-suspended in 100 mM TEAB buffer (100 μL). The TMT labeling reagents were equilibrated to room temperature, and anhydrous ACN (200 μL) was added to each reagent channel. Each channel was gently vortexed for 5 min, and then 20 μL from each TMT channel was transferred to the peptide solutions and allowed to incubate for 1 h at room temperature. All channels for each batch were then combined (batch 1 used all 11 channels, batch 2 utilized only 10 channel and batch 3 utilized only 8 channels) and dried by SpeedVac (LabConco) to approximately 150 μL and diluted with 1 mL of 0.1% (v/v) TFA, then acidified to a final concentration of 1% (v/v) FA and 0.1% (v/v) TFA. Peptides were desalted with a 200 mg C18 Sep-Pak column (Waters). Each Sep-Pak column was activated with 3 mL of methanol, washed with 3 mL of 50% (v/v) ACN, and equilibrated with 2 × 3 mL of 0.1% TFA. The samples were then loaded, and each column was washed with 2 × 3 mL 0.1% (v/v) TFA, followed by 2 mL of 1% (v/v) FA. Elution was performed with 2 volumes of 1.5 mL 50% (v/v) ACN. The eluates were then dried to completeness.

High pH fractionation

For batches 1 and 2, dried samples were re-suspended in high pH loading buffer (0.07% v/v NH_4OH, 0.045% v/v FA, 2% v/v ACN) and loaded onto an Agilent ZORBAX 300 Extend-C18 column (2.1 mm × 150 mm with 3.5 μm beads). An Agilent 1100 HPLC system was used to carry out the fractionation. Solvent A consisted of 0.0175% (v/v) NH4OH, 0.01125% (v/v) FA, and 2% (v/v) ACN; solvent B consisted of 0.0175% (v/v) NH4OH, 0.01125% (v/v) FA, and 90% (v/v) ACN. The sample elution was performed over a 58.6 min gradient with a flow rate of 0.4 mL/min. The gradient consisted of 100% solvent A for 2 min, then 0%–12% solvent B over 6 min, then 12% to 40% over 28 min, then 40%–44% over 4 min, then 44%–60% over 5 min, and then held constant at 60% solvent B for 13.6 min. A total of 96 individual equal volume fractions were collected across the gradient and subsequently pooled by concatenation into 24 fractions. For batch 3, dried samples were re-suspended in high pH loading buffer (0.07% v/v NH_4OH, 0.045% v/v FA, 2% v/v ACN) and loaded onto a Waters BEH 1.7 μm 2.1mm by 150mm. A Thermo Vanquish was used to carry out the fractionation. Solvent A consisted of 0.0175% (v/v) NH_4OH, 0.01125% (v/v) FA, and 2% (v/v) ACN; solvent B consisted of 0.0175% (v/v) NH_4OH, 0.01125% (v/v) FA, and 90% (v/v) ACN. The sample elution was performed over a 25 min gradient with a flow rate of 0.6 mL/min. A total of 192 individual equal volume fractions were collected across the gradient and subsequently pooled by concatenation into 96 fractions. All fractions were dried to completeness using a SpeedVac.

Liquid chromatography-tandem mass spectrometry

For batches 1 and 2, each of the 24 high-pH peptide fractions was resuspended in loading buffer (0.1% FA, 0.03% TFA, 1% ACN). Peptide eluents were separated on a self-packed C18 (1.9 μm Dr. Maisch, Germany) fused silica column (50 cm × 75 μM internal diameter (ID), New Objective, Woburn, MA) by an Easy nLC 1200 (Thermo Scientific) and monitored on a Q-Exactive HFX mass spectrometer (Thermo Scientific). Elution was performed over a 120-min gradient at a rate of 250 nL/min or 300 nL/min with buffer B

ranging from 3% to 50% (buffer A: 0.1% FA in water, buffer B: 0.1% FA in 80% ACN). For batch 1, the mass spectrometer was set to acquire data in positive ion mode using data-dependent acquisition with top 20 cycles. Each cycle consisted of one full MS scan followed by a maximum of 20 MS/MS. Full MS scans were collected at a resolution of 120,000 (400–1600 m/z range, 1 × 10^6 AGC, 100 ms maximum ion injection time). All higher energy collision-induced dissociation (HCD) MS/MS spectra were acquired at a resolution of 45,000 (1.6 m/z isolation width, 0.5 m/z offset, 32% collision energy, 1 × 10^4 AGC target, 86 ms maximum ion time). Dynamic exclusion was set to exclude previously sequenced peaks for 20 s within a 10-ppm isolation window. For batch 2, the mass spectrometer was set to acquire data in positive ion mode using data-dependent acquisition with top 10 cycles. Each cycle consisted of one full MS scan followed by a maximum of 10 MS/MS. Full MS scans were collected at a resolution of 120,000 (400–1600 m/z range, 3 × 10^6 AGC, 100 ms maximum ion injection time). All higher energy collision-induced dissociation (HCD) MS/MS spectra were acquired at a resolution of 45,000 (1.6 m/z isolation width, 0.5 m/z offset, 30% collision energy, 1 × 10^4 AGC target, 86 ms maximum ion time). Dynamic exclusion was set to exclude previously sequenced peaks for 20 s within a 10-ppm isolation window.

For batch 3, each of the 96 high-pH fractions was resuspended in loading buffer (0.1% FA, 0.03% TFA, 1% ACN). Peptide eluents were separated on a self-packed C18 (1.7 μm Water's BEH) fused silica column (laser pulled 15 cm × 150 μM ID) by Ultimate 3000 RSLCnano (Thermo Scientific). Elution was performed over a 36-min gradient at a rate of 1ul/min with buffer B ranging from 3% to 50% (buffer A: 0.1% FA in water, buffer B: 0.1% FA in 80% ACN). Mass spectrometry was performed with a high-field asymmetric waveform ion mobility spectrometry (FAIMS) Pro frontend equipped Orbitrap Eclipse (Thermo) in positive ion mode using data-dependent acquisition with 1.5 s top speed cycles for each FAIMS compensative voltage (CV). Each cycle consisted of one full MS scan followed by as many MS/MS events that could fit within the given 1.5 s cycle time limit. MS scans were collected at a resolution of 120,000 (410–1600 m/z range, 4 × 10^5 AGC, 50 ms maximum ion injection time, FAIMS CV of −45 and −65). Only precursors with charge states between 2+ and 6+ were selected for MS/MS. All higher energy collision-induced dissociation (HCD) MS/MS spectra were acquired at a resolution of 30,000 (0.7 m/z isolation width, 35% collision energy, 1.25^5 AGC target, 54 ms maximum ion time, turboTMT on). Dynamic exclusion was set to exclude previously sequenced peaks for 20 s within a 10-ppm isolation window.

Proteome identification and quantification with proteome discoverer

All raw files were analyzed using Proteome Discoverer v2.5.0.400 (ThermoFisher Scientific). MS/MS spectra were compared to theoretical spectra in a search performed by the Sequest HT search engine, with parameters specified as: fully tryptic specificity, a maximum of two missed cleavages, a minimum peptide length of six, fixed modifications for TMT or TMTPro tags on lysine residues and peptide N-termini (respectively +229.163 or +304.207 Da), carbamidomethylation of cysteine (+57.021 Da), and dynamic modification of methionine oxidation (+15.995 Da) and N-terminal protein loss of methionine, methionine loss plus acetylation, or acetylation (−131.040 Da, −89.030 Da, or +42.011 Da, respectively); precursor mass tolerance was 20 ppm, and Fragment tolerance 0.05 Da. The FASTA database searched was downloaded from UniProt on August 15, 2020, and contained 91,413 entries, plus one added for human amyloid beta residues 6–28 (HDSGYEVHHQKLVFFAEDVGSNK). Correction for stable isotope labeling impurity of the TMT tags used in each of the 3 batches was performed. Proteins reported in the consensus workflow were filtered by Percolator to 0.005 FDR-passed 1,266,002 PSMs, 0.01 FDR-passed 310,145 peptide groups, and 0.05 FDR-passed 49,656 proteins, including decoys in each case. Strict parsimony principles were followed to group peptides into proteins so that 11,681 protein parsimony groups represent the full results. A complete protein-level TMT reporter normalized abundance table is available (Table S3).

RNA extraction, sequencing and analyses for 18M mouse brains

RNA sequencing data for TgCRND8 transgenic mice was downloaded from Synapse (https://doi.org/10.7303/syn3157182). RNA was extracted using the RNeasy mini extraction kit with on-column DNase treatment (QIAGEN). RNA quantity is determined with the Qubit RNA HS assay. RNA quality will be checked via the RNA Integrity Number (RIN) on an Agilent Bioanalyzer 2100 with the Eukaryote Total RNA Nano chip. Libraries will be generated polyA enrichment using the Illumina TruSeq Stranded mRNA library prep kit. Libraries will be sequenced on paired-end, 100 bp runs on the Nextseq 2000 (Illumina) utilizing a pooling strategy that minimized batch effects from extraction, library preparation.

IFASTQ files were aligned against the mouse genome (GRCm39) and GRCm39.107 annotation using STAR[122] to generate BAM files. Gene counts were generated from BAM files using Rsamtools (https://bioconductor.org/packages/release/bioc/html/SummarizedExperiment.html) and the summarizeOverlaps function with the GenomicAlignments package v1.36.0.[123] Differential gene expression analysis was performed with DESeq2 package v1.40.2 using the "DESeq" function with default settings[124] which fits a generalized linear model for each gene. Subsequent Wald test P-values are adjusted for multiple comparisons using the Benjamini–Hochberg method (adjusted P-value). Pairwise changes in gene expression levels between groups were used to identify DEGs. DEGs will be defined as an absolute log2FC $\geq$ 0.5 and an adjusted P-value $\leq$0.05.IFASTQ files were aligned against the mouse genome (GRCm39) and GRCm39.107 annotation using STAR[122] to generate BAM files. Gene counts were generated from BAM files using Rsamtools (https://bioconductor.org/packages/release/bioc/html/SummarizedExperiment.html) and the summarizeOverlaps function with the GenomicAlignments package v1.36.0.[123] Differential gene expression analysis was performed with DESeq2 package v1.40.2 using the "DESeq" function with default settings[124] which fits a generalized linear model for each gene.

Subsequent Wald test P-values are adjusted for multiple comparisons using the Benjamini–Hochberg method (adjusted P-value). Pairwise changes in gene expression levels between groups were used to identify DEGs.

QUANTIFICATION AND STATISTICAL ANALYSIS

Data were analyzed statistically according to the methods specified in each figure legend. Briefly, *p* values were obtained as specified by either a one-way ANOVA test with two groups, or for enrichment, by a Fisher's Exact test. *p* values were corrected for multiple testing were indicated by Benjamini-Hochberg FDR correction. For significance of Pearson correlations, Student's test was used. GraphPad Prism 9.5.1 was used for statistical analysis and graph creation.

Bioinformatic analyses

Circular heatmap plot of eigenprotein-trait correlations (bicor), native eigenprotein -$\log_{10}$(p) for signed significance of AD vs. control or synthetic eigenprotein Tg vs. WT comparison, and the -$\log_{10}$(BH FDR) of cell type marker enrichment from the one-tailed Fisher's test *p* value was visualized using the R circlize package suite of functions using an in-house script. Synthetic eigenprotein calculations used the top 20 percent of hubs ranked by kME, a minimum of 4 hubs per module, calculating the first principal component of variance in those hubs[8] after mapping cross-species using the biomaRt R package getLDS function. Effect size correlation plots leveraged the WGCNA verboseScatterplot function for Pearson rho, least squares fit line, and Student's significance of the Pearson correlation. Boxplots were drawn using the base R boxplot function, with individual points overlain using the beeswarm package function of the same name. The stacked bar plot of percent differentially expressed proteins per module was executed using the DEXpercentStacked function available from https://www.github.com/edammer/parANOVA/. Ensemble human AD GWAS MAGMA *p* values (Table S1) were determined as the mean -$\log_{10}$(p) gene-level risk for all genes reaching nominal significance in any of the three GWAS studies considered,[49–51] following rollup of SNP-level GWAS summary statistics to the gene-level *p* value using MAGMA v1.09b. *p* values were calculated using one-way ANOVA statistics in R v4.2.3, e.g., for eigenprotein groupwise comparisons, unless otherwise noted.

Gene ontology analyses

Gene ontology enrichment analysis were performed with goseq[125] to identify enrichment in gene ontology categories and KEGG pathways. For DEGs, up- and down-regulated gene lists will be analyzed separately. For WGCNA, gene lists from each module will be used as input. Over-represented P-values will be adjusted for multiple comparisons using the Benjamini–Hochberg (BH) adjustments for controlling false-discovery rates. An enrichment score will be calculated using an observed-over-expected ratio for each gene list. GO-BP categories and KEGG pathways were plotted if their BH adjusted FDR reached $\geq$ 0.05 and the number of DEGs within each category/pathway was greater than 4. Individual GO terms were grouped based on their similarity of gene composition computed using the Jaccard similarity index where J(A, B) = |size of A intersection B|/|size of A union B|. These groupings were then expert annotated based on the overarching main function and theme of their constituent members into supergroups. The mean enrichment and *p*-values for the union of all member GO terms for each supergroup were calculated for graphing.